

Stress-hybrid virtual element method on six-noded triangular meshes for compressible and nearly-incompressible linear elasticity

Alvin Chen^a, Joseph E. Bishop^b, N. Sukumar^{c,*}

^a*Department of Mathematics, University of California, Davis, 95616, CA, USA*

^b*Engineering Sciences Center, Sandia National Laboratories, Albuquerque, 87185, NM, USA*

^c*Department of Civil and Environmental Engineering, University of California, Davis, 95616, CA, USA*

Abstract

In this paper, we present a first-order Stress-Hybrid Virtual Element Method (SH-VEM) on six-noded triangular meshes for linear plane elasticity. We adopt the Hellinger–Reissner variational principle to construct a weak equilibrium condition and a stress based projection operator. On applying the divergence theorem to the weak strain-displacement relations, the stress projection operator is expressed in terms of the nodal displacements, which leads to a displacement-based formulation. This stress-hybrid approach assumes a globally continuous displacement field while the stress field is discontinuous across each element. The stress field is initially represented by divergence-free tensor polynomials based on Airy stress functions. However, for flexibility in choosing basis functions, we also present a formulation that uses a penalty term to enforce the element equilibrium conditions. This method is referred to as the Penalty Stress-Hybrid Virtual Element Method (PSH-VEM). Numerical results are presented for PSH-VEM and SH-VEM, and we compare their convergence to the composite triangle FEM and B-bar VEM on benchmark problems in linear elasticity. The SH-VEM converges optimally in the L^2 norm of the displacement, energy seminorm, and the L^2 norm of hydrostatic stress. Furthermore, the results reveal that PSH-VEM converges in most cases at a faster rate than the expected optimal rate, but it requires the selection of a suitably chosen penalty parameter.

Keywords: stabilization-free virtual element method, triangular meshes, hexagonal meshes, Hellinger–Reissner variational principle, volumetric locking, shear locking

1. Introduction

In many applications of the finite element method, quadrilaterals and hexahedra are the standard elements that are used. However, high-quality quadrilateral and hexahedral meshes cannot be automatically generated for complex geometries. Triangular and tetrahedral meshes have well-established automatic mesh generators, but these elements tend to be overly stiff and suffer from volumetric locking in the nearly-incompressible limit. Many techniques such as the B-bar and selective integration formulations [46, 55], method of incompatible modes [70], assumed enhanced strain [61, 62], stabilized elements [9, 10], mixed

*Corresponding authors

Email address: nsukumar@ucdavis.edu (N. Sukumar)

elements [75], and hybrid stress methods [36, 37, 38, 51, 52, 53] have been developed to alleviate locking in the nearly-incompressible limit. However, many of these methods are only applicable to quadrilateral and hexahedral elements. Progress has been made to construct modified triangular elements that are robust and accurate: the variational multiscale approach [58], hybrid-stress elements using Airy stress functions [40, 43, 45, 57, 68], Bézier elements [39], F-bar and reduced integration [27, 47] to name a few. Another promising approach is the use of composite elements [14, 32, 34, 42, 48, 66]. In this approach, an element is split into sub-triangles (sub-tetrahedra), and then on each sub-triangle the strain is approximated and combined to recover the strain field over the entire element. Similar constructions are also used in [13] to construct a three-dimensional brick element for nearly incompressible nonlinear elasticity problems and in [23, 24, 25, 30] for triangular bending elements.

The recent development of the virtual element method [6, 7, 8] has provided an alternative way to extend these methods to alleviate volumetric locking for general polygons and polyhedra. Methods such as mixed and hybrid formulations [3, 5, 26, 28], B-bar [49], assumed strain [11, 18, 19, 29, 41], and recently hybrid stress for general quadrilaterals [20] have been adopted in the virtual element method. The approach of using triangular sub-elements has also been applied in [71] to construct a stabilization term for the virtual element method.

In this paper, we focus on nearly-incompressible two-dimensional linear elasticity problems; however, extensions to three-dimensional problems appears to be feasible. We first propose a virtual element method for a six-noded element using equilibrated stress fields originally motivated for finite elements in [17, 51, 64]. This method is applicable to both convex and nonconvex elements; however, in our application we focus mainly on triangular meshes with an additional node placed along each edge of the triangle. Following [20], we refer to this approach as the Stress-Hybrid Virtual Element Method (SH-VEM). This approach draws on the stress-hybrid finite element method of Pian and Sumihara [52] and the resulting method resembles the stress recovery procedure of Artioli et al. [4]. Unlike the standard mixed or hybrid methods based on the Hellinger–Reissner principle, which require the use of more specialized approximation spaces and additional traction degrees of freedom, the stress-hybrid approach uses a discontinuous stress field that is only dependent on the nodal displacement degrees of freedom. When using a fifteen-parameter expansion, the resulting method does not require a stabilization term and shows immunity to shear and volumetric locking.

The remainder of this paper is structured as follows. In Section 2, we use the Hellinger–Reissner variational principle to construct a weak formulation of the linear elasticity problem. In Section 3, we construct the necessary projection operators and present the virtual element space. In Section 4, we present the numerical implementation of the projections, discuss possible choices of stress basis functions, and construct the element stiffness matrix. A difficulty with the stress-hybrid approach is the need to construct a suitable basis for the stress field. In the previous sections, we utilized stress expansions derived from the Airy stress functions; however, it is difficult to find these stress functions for anisotropic and nonlinear materials or for three-dimensional problems. In Section 5, we present a virtual element method that combines the stress-hybrid VEM with an equilibrium penalty term in order to construct an element that does not rely on the Airy stress functions, alleviates shear locking, and requires no stabilization term. We refer to this formulation as the Penalty

Stress-Hybrid Virtual Element Method (PSH-VEM). In Section 6, we present numerical results for Composite Triangle FEM (CT FEM) [34], B-bar VEM [49], SH-VEM, and PSH-VEM. We first present an eigenvalue analysis to determine the stability of the different methods and the suitability of different stress basis functions. Then we present results for the four methods on a series of benchmark problems in plane strain linear elasticity in the nearly-incompressible limit: bending of a thin cantilever beam, Cook’s membrane, infinite plate with a circular hole, hollow pressurized cylinder, a manufactured problem with exact solution, and the punch problem. We close with our main findings and some final remarks in Section 7.

2. Variational formulation

Consider an elastic body occupying a bounded region $\Omega \subset \mathbb{R}^2$. Assume that the boundary $\partial\Omega$ can be decomposed into a disjoint union $\partial\Omega = \Gamma_u \cup \Gamma_t$ and $\Gamma_u \cap \Gamma_t = \emptyset$. On Γ_u , displacement boundary conditions $\mathbf{u} = \mathbf{u}_0$ are imposed, while tractions $\mathbf{t} = \bar{\mathbf{t}}$ are applied on Γ_t . The displacement field is denoted by $\mathbf{u} \in [H^1(\Omega)]^2$, the small-strain tensor $\boldsymbol{\varepsilon} = \nabla_s \mathbf{u}$, the Cauchy stress tensor $\boldsymbol{\sigma} \in [L^2(\Omega)]_{\text{sym}}^{2 \times 2}$, the material moduli tensor is \mathbb{C} , and $\mathbf{b} \in [L^2(\Omega)]^2$ represents the body force per unit volume.

Following [20], we introduce the Hellinger–Reissner functional for linear elasticity:

$$\Pi_{\text{HR}}[\mathbf{u}, \boldsymbol{\sigma}] = -\frac{1}{2} \int_{\Omega} \boldsymbol{\sigma} : \mathbb{C}^{-1} : \boldsymbol{\sigma} \, d\mathbf{x} + \int_{\Omega} \boldsymbol{\sigma} : \nabla_s \mathbf{u} \, d\mathbf{x} - \int_{\Omega} \mathbf{b} \cdot \mathbf{u} \, d\mathbf{x} - \int_{\Gamma_t} \bar{\mathbf{t}} \cdot \mathbf{u} \, ds.$$

After taking the first variation of $\Pi_{\text{HR}}(\cdot, \cdot)$ and requiring it to be stationary, we obtain the weak statement of the equilibrium equations and strain-displacement relations:

$$\int_{\Omega} \boldsymbol{\sigma} : \nabla_s(\delta \mathbf{u}) \, d\mathbf{x} - \int_{\Omega} \mathbf{b} \cdot \delta \mathbf{u} \, d\mathbf{x} - \int_{\Gamma_t} \bar{\mathbf{t}} \cdot \delta \mathbf{u} \, ds = 0 \quad \forall \delta \mathbf{u} \in \mathcal{V}_u, \quad (1a)$$

$$\int_{\Omega} \delta \boldsymbol{\sigma} : (\nabla_s \mathbf{u} - \mathbb{C}^{-1} : \boldsymbol{\sigma}) \, d\mathbf{x} = 0 \quad \forall \delta \boldsymbol{\sigma} \in \mathcal{V}_{\sigma}, \quad (1b)$$

where $\mathcal{V}_u \subset [H^1(\Omega)]^2$ contains vector-valued functions that vanish on Γ_u and \mathcal{V}_{σ} contains symmetric tensor-valued functions in $[L^2(\Omega)]_{\text{sym}}^{2 \times 2}$.

3. Stress-hybrid virtual element discretization

In this section, we introduce the projection operations used in the virtual element method. In the virtual element method, the polygonal basis functions are not explicitly constructed and only known on the boundary of an element; therefore, projection operators are needed to represent the displacement and stress fields in the interior of elements. We first define the energy projection of the displacement field using an energy orthogonality condition. Next, we define the stress-hybrid projection using the orthogonality condition based on the weak strain-displacement relation obtained from the Hellinger–Reissner principle. Finally, we define the virtual element space and the virtual basis functions over a single element.

Let \mathcal{T}^h be a decomposition of Ω into six-noded elements (see Figure 1). For each element E , denote the diameter by h_E , its centroid by \mathbf{x}_E and the coordinate of the i -th vertex by $\mathbf{x}_i = (x_i, y_i)$.

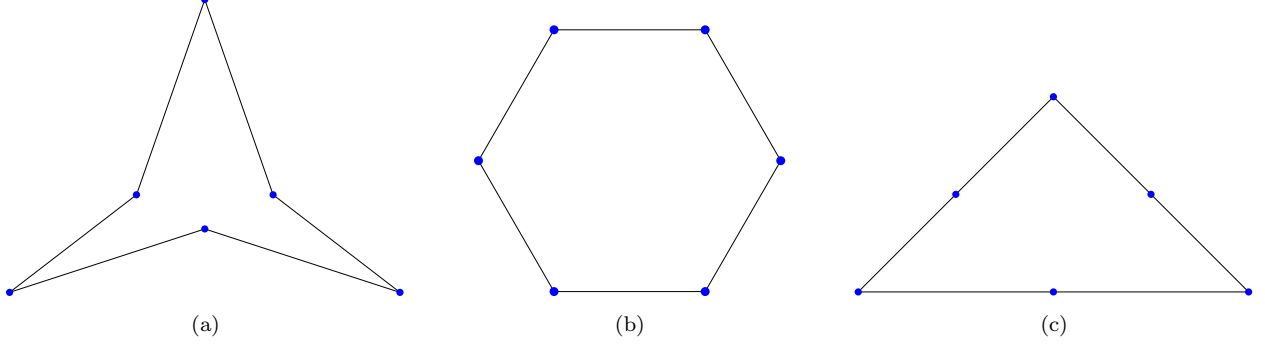


Figure 1: Examples of admissible six-noded elements (a) nonconvex element, (b) hexagonal element and (c) six-noded triangular element.

3.1. Energy projection operator of the displacement field

For the displacement field approximation in each element, we choose a basis of first order scaled vector monomials given by:

$$\widehat{\mathbf{M}}(E) = \left[\begin{array}{c} \left\{ \begin{array}{c} 1 \\ 0 \end{array} \right\}, \left\{ \begin{array}{c} 0 \\ 1 \end{array} \right\}, \left\{ \begin{array}{c} -\eta \\ \xi \end{array} \right\}, \left\{ \begin{array}{c} \eta \\ \xi \end{array} \right\}, \left\{ \begin{array}{c} \xi \\ 0 \end{array} \right\}, \left\{ \begin{array}{c} 0 \\ \eta \end{array} \right\} \end{array} \right], \quad (2a)$$

where

$$\xi = \frac{x - x_E}{h_E}, \quad \eta = \frac{y - y_E}{h_E}. \quad (2b)$$

Let \mathbf{m}_α denote the α th column of $\widehat{\mathbf{M}}(E)$, and define $\widetilde{\mathbf{M}}$ as the matrix representation given by

$$\widetilde{\mathbf{M}} = \begin{bmatrix} 1 & 0 & -\eta & \eta & \xi & 0 \\ 0 & 1 & \xi & \xi & 0 & \eta \end{bmatrix}. \quad (2c)$$

Then for each element E , define the energy projection of the displacement field $\Pi^\varepsilon : [H^1(E)]^2 \rightarrow [\mathbb{P}_1(E)]^2$ as a function that satisfies the energy orthogonality condition:

$$\int_E \boldsymbol{\varepsilon}(\mathbf{m}_\alpha) : \mathbb{C} : \boldsymbol{\varepsilon}(\mathbf{v} - \Pi^\varepsilon \mathbf{v}) \, d\mathbf{x} = 0 \quad \forall \mathbf{m}_\alpha \in \widehat{\mathbf{M}}(E). \quad (3)$$

For $\alpha = 1, 2, 3$, \mathbf{m}_α correspond to rigid-body modes, so we get $\boldsymbol{\varepsilon}(\mathbf{m}_\alpha) = 0$. This results in three trivial equations $0 = 0$, and therefore we require three additional conditions to define a unique projection. Let $Q_0 : [H^1(E)]^2 \times [H^1(E)]^2 \rightarrow \mathbb{R}$ be the discrete L^2 inner product:

$$Q_0(\mathbf{u}, \mathbf{v}) = \frac{1}{6} \sum_{k=1}^6 \mathbf{u}(\mathbf{x}_k) \cdot \mathbf{v}(\mathbf{x}_k), \quad (4a)$$

and then impose the additional three constraints on $\Pi^\varepsilon \mathbf{v}$:

$$Q_0(\mathbf{m}_\alpha, \mathbf{v} - \Pi^\varepsilon \mathbf{v}) = \frac{1}{6} \sum_{k=1}^6 \mathbf{m}_\alpha(\mathbf{x}_k) \cdot (\mathbf{v} - \Pi^\varepsilon \mathbf{v})(\mathbf{x}_k) = 0 \quad (\alpha = 1, 2, 3). \quad (4b)$$

The condition (4b) enforces the nodal average of \mathbf{v} and its projection $\Pi^\varepsilon \mathbf{v}$ for a rigid-body mode to be equal. Now we define the energy projection $\Pi^\varepsilon \mathbf{v}$ as the unique function that satisfies the following two relations:

$$\frac{1}{6} \sum_{k=1}^6 \mathbf{m}_\alpha(\mathbf{x}_k) \cdot (\mathbf{v} - \Pi^\varepsilon \mathbf{v})(\mathbf{x}_k) = 0 \quad (\alpha = 1, 2, 3), \quad (5a)$$

$$\int_E \boldsymbol{\varepsilon}(\mathbf{m}_\alpha) : \mathbb{C} : \boldsymbol{\varepsilon}(\mathbf{v} - \Pi^\varepsilon \mathbf{v}) \, d\mathbf{x} = 0 \quad (\alpha = 4, 5, 6). \quad (5b)$$

For implementation, it is more convenient to write (5b) in matrix-vector form. From [19], this relation can be written as

$$\int_E (\mathbf{S}\Pi^\varepsilon \mathbf{v})^T (\mathbf{C}\mathbf{S}\mathbf{m}_\alpha) \, d\mathbf{x} = \int_E (\mathbf{S}\mathbf{v})^T (\mathbf{C}\mathbf{S}\mathbf{m}_\alpha) \, d\mathbf{x}, \quad (6a)$$

where \mathbf{S} is the matrix symmetric gradient operator that is given by

$$\mathbf{S} = \begin{bmatrix} \frac{\partial}{\partial x} & 0 \\ 0 & \frac{\partial}{\partial y} \\ \frac{\partial}{\partial y} & \frac{\partial}{\partial x} \end{bmatrix}, \quad (6b)$$

and \mathbf{C} is the matrix representation of the material moduli tensor. For our study, we assume that the material is homogeneous, isotropic and linearly elastic. We also use the plane strain condition since we are interested in applications when the material is nearly incompressible. Under these assumptions, the matrix \mathbf{C} is given by

$$\mathbf{C} = \frac{E_Y}{(1+\nu)(1-2\nu)} \begin{bmatrix} 1-\nu & \nu & 0 \\ \nu & 1-\nu & 0 \\ 0 & 0 & \frac{1-2\nu}{2} \end{bmatrix}, \quad (6c)$$

where E_Y is the Young's modulus and ν is the Poisson's ratio of the material.

3.2. Stress-hybrid projection operator

Let $\ell \in \mathbb{Z}_{\geq 0}$ be the largest degree polynomial used for the stress approximation on an element. Then following [20], define the projection operator $\Pi_\beta \boldsymbol{\sigma}$ for the stress-hybrid formulation by the condition

$$\int_E \mathbb{P} : (\nabla_s \mathbf{u} - \mathbb{C}^{-1} : \Pi_\beta \boldsymbol{\sigma}) \, d\mathbf{x} = 0 \quad \forall \mathbb{P} \in [\mathbb{P}_\ell(E)]_{\text{sym}}^{2 \times 2},$$

which is rewritten as

$$\int_E \mathbb{P} : \mathbb{C}^{-1} : \Pi_\beta \boldsymbol{\sigma} \, d\mathbf{x} = \int_E \mathbb{P} : \nabla_s \mathbf{u} \, d\mathbf{x} \quad \forall \mathbb{P} \in [\mathbb{P}_\ell(E)]_{\text{sym}}^{2 \times 2}.$$

Now applying the divergence theorem and simplifying, we obtain

$$\int_E \mathbb{P} : \mathbb{C}^{-1} : \Pi_\beta \boldsymbol{\sigma} \, d\mathbf{x} = \int_{\partial E} (\mathbb{P} \cdot \mathbf{n}) \cdot \mathbf{u} \, ds - \int_E (\nabla \cdot \mathbb{P}) \cdot \mathbf{u} \, d\mathbf{x}, \quad (8)$$

Let $\overline{\mathbb{P}}$, $\overline{\Pi_\beta \boldsymbol{\sigma}}$ be the Voigt representation of \mathbb{P} and $\Pi_\beta \boldsymbol{\sigma}$, respectively. Then, (8) can be written as

$$\int_E \overline{\mathbb{P}}^T \mathbf{C}^{-1} \overline{\Pi_\beta \boldsymbol{\sigma}} d\mathbf{x} = \int_{\partial E} \overline{\mathbb{P}}^T \mathbf{N}^{\partial E} \mathbf{u} ds - \int_E (\boldsymbol{\partial} \overline{\mathbb{P}})^T \mathbf{u} d\mathbf{x} \quad \forall \mathbb{P} \in [\mathbb{P}_\ell(E)]_{\text{sym}}^{2 \times 2}, \quad (9a)$$

where $\mathbf{N}^{\partial E}$ is the matrix representation of the outward normals along the boundary of E , and $\boldsymbol{\partial}$ is the matrix divergence operator that are given by

$$\mathbf{N}^{\partial E} := \begin{bmatrix} n_x & 0 \\ 0 & n_y \\ n_y & n_x \end{bmatrix}, \quad \boldsymbol{\partial} := \begin{bmatrix} \frac{\partial}{\partial x} & 0 & \frac{\partial}{\partial y} \\ 0 & \frac{\partial}{\partial y} & \frac{\partial}{\partial x} \end{bmatrix}. \quad (9b)$$

3.3. Virtual element space

In the standard first order virtual element method [6], the virtual element space consists of harmonic functions that are piecewise affine and continuous along the boundary of an element. On each vertex of the element, there are two displacement degrees of freedom, which allows for the construction of a linear projection operator of the displacement field and a constant projection operator of the stress field. However, this space is not sufficient to compute the projection $\overline{\Pi_\beta \boldsymbol{\sigma}}$ for arbitrary ℓ without adding additional degrees of freedom; therefore, we follow the approach of [11, 19] to define the first order enlarged (enhanced) virtual element space for each element E :

$$\mathbf{V}(E) = \left\{ \mathbf{v}_h \in [H^1(E)]^2 : \Delta \mathbf{v}_h \in [\mathbb{P}_{\ell-1}(E)]^2, \mathbf{v}_h|_e \in [\mathbb{P}_1(e)]^2 \forall e \in \partial E, \right. \\ \left. \mathbf{v}_h|_{\partial E} \in [C^0(\partial E)]^2, \int_E \mathbf{v}_h \cdot \mathbf{p} d\mathbf{x} = \int_E \Pi^\varepsilon \mathbf{v}_h \cdot \mathbf{p} d\mathbf{x} \quad \forall \mathbf{p} \in [\mathbb{P}_{\ell-1}(E)]^2 \right\}, \quad (10)$$

where Δ is the vector Laplacian operator and e is an edge of the element. For each element E we also assign a basis for the local space $\mathbf{V}(E)$. Let $\{\phi_i\}$ be the scalar polygonal basis functions in standard VEM [6] that satisfy the Kronecker-delta property $\phi_i(\mathbf{x}_j) = \delta_{ij}$. Using the scalar basis, we define the matrix of vector-valued basis functions by

$$\boldsymbol{\varphi} = \begin{bmatrix} \phi_1 & \phi_2 & \phi_3 & \cdots & \phi_6 & 0 & 0 & 0 & \cdots & 0 \\ 0 & 0 & 0 & \cdots & 0 & \phi_1 & \phi_2 & \phi_3 & \cdots & \phi_6 \end{bmatrix} := [\boldsymbol{\varphi}_1 \quad \boldsymbol{\varphi}_2 \quad \cdots \quad \boldsymbol{\varphi}_{12}], \quad (11a)$$

then any function $\mathbf{v}_h \in \mathbf{V}(E)$ can be represented as:

$$\mathbf{v}_h(\mathbf{x}) = \sum_{i=1}^{12} \boldsymbol{\varphi}_i(\mathbf{x}) v_i = \boldsymbol{\varphi} \mathbf{d}, \quad (11b)$$

where v_i is the i -th degree of freedom of \mathbf{v}_h .

4. Stress-hybrid implementation

With the definition of the projection operators and the virtual element space, we now present the implementation of the stress-hybrid virtual element method. We first construct the energy projection and discuss different choices of stress basis when constructing the stress-hybrid projection. We then build the element stiffness matrix and the element force vector.

4.1. Implementation of the energy projection

We follow the construction of the energy projection from [19]. Let $\mathbf{v}_h = \boldsymbol{\varphi}_i$ be the i -th basis function ($i = 1, 2, \dots, 12$) of $\mathbf{V}(E)$, then after substituting into (5a) and (6a), the energy projection $\Pi^\varepsilon \boldsymbol{\varphi}_i$ is given by the two relations:

$$\frac{1}{6} \sum_{k=1}^6 \mathbf{m}_\alpha(\mathbf{x}_k) \cdot \Pi^\varepsilon \boldsymbol{\varphi}_i(\mathbf{x}_k) = \frac{1}{6} \sum_{k=1}^6 \mathbf{m}_\alpha(\mathbf{x}_k) \cdot \boldsymbol{\varphi}_i(\mathbf{x}_k) \quad (\alpha = 1, 2, 3), \quad (12a)$$

$$\int_E (\mathbf{S} \Pi^\varepsilon \boldsymbol{\varphi}_i)^T (\mathbf{C} \mathbf{S} \mathbf{m}_\alpha) d\mathbf{x} = \int_E (\mathbf{S} \boldsymbol{\varphi}_i)^T (\mathbf{C} \mathbf{S} \mathbf{m}_\alpha) d\mathbf{x} \quad (\alpha = 4, 5, 6). \quad (12b)$$

The projection $\Pi^\varepsilon \boldsymbol{\varphi}_i$ is an affine vector polynomial, therefore we expand it in terms of the basis in (2a). That is:

$$\Pi^\varepsilon \boldsymbol{\varphi}_i = \sum_{\mu=1}^6 (\mathbf{\Pi}_*^\varepsilon)_{\mu i} \mathbf{m}_\mu \quad (i = 1, 2, \dots, 12).$$

After substituting in (12) and simplifying, we obtain the energy projection coefficients $\mathbf{\Pi}_*^\varepsilon$ as [19]

$$\mathbf{\Pi}_*^\varepsilon = \mathbf{G}^{-1} \mathbf{B}, \quad (13a)$$

where for $\mu = 1, 2, \dots, 6$

$$\mathbf{G}_{\alpha\mu} = \begin{cases} \frac{1}{6} \sum_{j=1}^6 \mathbf{m}_\mu(\mathbf{x}_j) \cdot \mathbf{m}_\alpha(\mathbf{x}_j) & (\alpha = 1, 2, 3) \\ \int_E (\mathbf{S} \mathbf{m}_\mu)^T (\mathbf{C} \mathbf{S} \mathbf{m}_\alpha) d\mathbf{x} & (\alpha = 4, 5, 6), \end{cases} \quad (13b)$$

and for $i = 1, 2, \dots, 12$

$$\mathbf{B}_{\alpha i} = \begin{cases} \frac{1}{6} \sum_{j=1}^6 \boldsymbol{\varphi}_i(\mathbf{x}_j) \cdot \mathbf{m}_\alpha(\mathbf{x}_j) & (\alpha = 1, 2, 3) \\ \int_E (\mathbf{S} \boldsymbol{\varphi}_i)^T (\mathbf{C} \mathbf{S} \mathbf{m}_\alpha) d\mathbf{x} & (\alpha = 4, 5, 6). \end{cases} \quad (13c)$$

4.2. Choice of stress basis for a hybrid formulation

It is known that for a stress-based method, using a stress approximation that satisfies the element equilibrium condition results in more accurate stress distributions for homogeneous problems [35, 63, 64, 72]. For plane isotropic elasticity, a convenient set of suitable stresses that satisfy the equilibrium equations with zero body force are derived from the Airy

stress functions [17, 33, 57]. A collection of fifteen potential stress fields is given in Voigt representation by [17]:

$$\mathbf{P} = \begin{bmatrix} 1 & 0 & 0 & \eta & \xi & 0 & 0 & 2\xi\eta & -\eta^2 & \xi^2 - \eta^2 & \xi(\xi^2 - 6\eta^2) & \xi^3 & 3\xi^2\eta & \eta(3\xi^2 - 2\eta^2) \\ 0 & 1 & 0 & 0 & \xi & 0 & \eta & 2\xi\eta & 0 & \xi^2 & \eta^2 - \xi^2 & 3\xi\eta^2 & -\xi(2\xi^2 - 3\eta^2) & -\eta(6\xi^2 - \eta^2) & \eta^3 \\ 0 & 0 & 1 & 0 & 0 & -\eta & -\xi & -\xi^2 & -\eta^2 & 0 & -2\xi\eta & -\eta(3\xi^2 - 2\eta^2) & -3\xi^2\eta & \xi(2\xi^2 - 3\eta^2) & -3\xi\eta^2 \end{bmatrix}. \quad (14)$$

For a six-noded element, there are twelve displacement degrees of freedom and three rigid-body modes, so a minimum of nine terms are needed for the stress approximation [54]. However, it is also known that using an incomplete stress approximation will result in a stiffness matrix that is not rotationally invariant [22, 52], or result in elements with inaccurate stress distributions [72]. Therefore, we only consider the complete bases with the first eleven terms of (14) and all fifteen terms. We denote any stress basis with k independent terms by $k\beta$.

Remark 1. The set of stress basis in (14) is an extension of the 5β hybrid-stress basis introduced in [51] and the 15β basis introduced in [64]. In [29], a similar collection of divergence-free polynomials is used as a basis for the enhanced strain VEM.

We also examine a basis similar to the hybrid basis given in [29], which uses a mix of nine uncoupled constant and linear polynomials and four divergence-free quadratic polynomials:

$$\mathbf{P}^* = \begin{bmatrix} 1 & 0 & 0 & \xi & 0 & 0 & \eta & 0 & 0 & 0 & 2\xi\eta & -\eta^2 & \xi^2 - \eta^2 \\ 0 & 1 & 0 & 0 & \xi & 0 & 0 & \eta & 0 & 2\xi\eta & 0 & \xi^2 & \eta^2 - \xi^2 \\ 0 & 0 & 1 & 0 & 0 & \xi & 0 & 0 & \eta & -\xi^2 & -\eta^2 & 0 & -2\xi\eta \end{bmatrix}. \quad (15)$$

4.3. Implementation of the stress-hybrid projection

We have the discrete relation of (9a) given by:

$$\int_E \overline{\mathbb{P}}^T \mathbf{C}^{-1} \overline{\Pi_\beta \boldsymbol{\sigma}} \, d\mathbf{x} = \int_{\partial E} \overline{\mathbb{P}}^T \mathbf{N}^{\partial E} \mathbf{u}_h \, ds - \int_E (\boldsymbol{\partial} \overline{\mathbb{P}})^T \mathbf{u}_h \, d\mathbf{x}. \quad (16a)$$

The last term in (16a) is not computable for general $\overline{\mathbb{P}}$; however since the elements of $\boldsymbol{\partial} \overline{\mathbb{P}}$ are polynomials of degree at most $\ell - 1$, we apply the definition of the virtual element space (10) to rewrite as

$$\int_E \overline{\mathbb{P}}^T \mathbf{C}^{-1} \overline{\Pi_\beta \boldsymbol{\sigma}} \, d\mathbf{x} = \int_{\partial E} \overline{\mathbb{P}}^T \mathbf{N}^{\partial E} \mathbf{u}_h \, ds - \int_E (\boldsymbol{\partial} \overline{\mathbb{P}})^T \Pi^\varepsilon \mathbf{u}_h \, d\mathbf{x}. \quad (16b)$$

Expanding \mathbf{u}_h in terms of the basis in $\mathbf{V}(E)$, we have $\mathbf{u}_h = \boldsymbol{\varphi} \mathbf{d}$, where \mathbf{d} is the displacement vector. We also expand $\overline{\Pi_\beta \boldsymbol{\sigma}}$ in terms of \mathbf{P} : $\overline{\Pi_\beta \boldsymbol{\sigma}} = \mathbf{P} \boldsymbol{\beta}$, and since $\overline{\mathbb{P}}$ is arbitrary we take $\overline{\mathbb{P}} = \mathbf{P}_i$ ($i = 1, 2, \dots, 15$). After substituting in (16b) for each $i = 1, 2, \dots, 15$ and simplifying, we obtain the system:

$$\left(\int_E \mathbf{P}^T \mathbf{C}^{-1} \mathbf{P} \, d\mathbf{x} \right) \boldsymbol{\beta} = \left(\int_{\partial E} \mathbf{P}^T \mathbf{N}^{\partial E} \boldsymbol{\varphi} \, ds - \int_E (\boldsymbol{\partial} \mathbf{P})^T \Pi^\varepsilon \boldsymbol{\varphi} \, d\mathbf{x} \right) \mathbf{d}. \quad (17)$$

For any choice of \mathbf{P} in (14), we have the divergence-free condition $\boldsymbol{\partial} \mathbf{P} = \mathbf{0}$, so we obtain

$$\left(\int_E \mathbf{P}^T \mathbf{C}^{-1} \mathbf{P} \, d\mathbf{x} \right) \boldsymbol{\beta} = \left(\int_{\partial E} \mathbf{P}^T \mathbf{N}^{\partial E} \boldsymbol{\varphi} \, ds \right) \mathbf{d}. \quad (18)$$

Now define the corresponding matrices \mathbf{H} and \mathbf{L} by

$$\mathbf{H} = \int_E \mathbf{P}^T \mathbf{C}^{-1} \mathbf{P} d\mathbf{x}, \quad \mathbf{L} = \int_{\partial E} \mathbf{P}^T \mathbf{N}^{\partial E} \boldsymbol{\varphi} ds. \quad (19a)$$

Since \mathbf{P} has linearly independent columns and \mathbf{C}^{-1} is symmetric positive-definite, the matrix \mathbf{H} is invertible. Then the stress coefficients are given by

$$\boldsymbol{\beta} = \mathbf{H}^{-1} \mathbf{L} \mathbf{d} := \boldsymbol{\Pi}_\beta \mathbf{d}, \quad (19b)$$

where $\boldsymbol{\Pi}_\beta$ is the matrix representation of the stress-hybrid projection operator with respect to the symmetric tensor polynomial basis \mathbf{P} .

Remark 2. For a nondivergence-free basis, the use of (16b) can lead to an overly stiff element. An alternate approach used in [29, 41], is to introduce additional internal moment degrees of freedom to compute the last integral in (16a). These additional DOFs result in better performing elements but require an additional static condensation on the element stiffness matrix. Another approach is to follow the idea of using composite elements [34] to compute the stress projection operator. For each element, we construct a sub-triangulation and assume the displacement field (displacement projection) is affine on each subtriangle. This piecewise displacement field can then be used to compute the integral in (16a). We tested a virtual element formulation based on composite elements and found that the resulting elements were more flexible but still suffered from volumetric locking.

4.4. Element stiffness and forcing

Following [20], we define the discrete system:

$$a_h^E(\mathbf{u}_h, \delta \mathbf{u}_h) = \ell_h^E(\delta \mathbf{u}_h),$$

where

$$\begin{aligned} a_h^E(\mathbf{u}_h, \delta \mathbf{u}_h) &:= \int_E \overline{\boldsymbol{\Pi}_\beta \boldsymbol{\sigma}(\delta \mathbf{u}_h)^T} \mathbf{C}^{-1} \overline{\boldsymbol{\Pi}_\beta \boldsymbol{\sigma}(\mathbf{u}_h)} d\mathbf{x}, \\ \ell_h^E(\delta \mathbf{u}_h) &:= \int_E (\delta \mathbf{u}_h)^T \mathbf{b} d\mathbf{x} + \int_{\Gamma_t \cap \partial E} (\delta \mathbf{u}_h)^T \bar{\mathbf{t}} ds. \end{aligned}$$

After expanding $\overline{\boldsymbol{\Pi}_\beta \boldsymbol{\sigma}}$ and simplifying, we construct the element stiffness matrix

$$\mathbf{K}_E = (\boldsymbol{\Pi}_\beta)^T \left(\int_E \mathbf{P}^T \mathbf{C}^{-1} \mathbf{P} d\mathbf{x} \right) \boldsymbol{\Pi}_\beta = \boldsymbol{\Pi}_\beta^T \mathbf{H} \boldsymbol{\Pi}_\beta. \quad (21)$$

Similarly, for every element E , the element force vector is given by

$$\mathbf{f}_E := \int_E \boldsymbol{\varphi}^T \mathbf{b} d\mathbf{x} + \int_{\Gamma_t \cap \partial E} \boldsymbol{\varphi}^T \bar{\mathbf{t}} ds. \quad (22)$$

5. Equilibrium penalty stress-hybrid method

Finding a basis that satisfies the equilibrium equations directly is difficult for nonlinear and anisotropic problems. From our tests, we also found that using only equilibrated basis functions requires many higher order functions and more terms than the optimal basis to retain stability, which results in stiffer solutions and greater integration costs. We examine an approach by [72], which uses a penalty term to weakly enforce the element equilibrium equations. The penalty formulation was originally shown to mitigate shear locking in the Pian-Sumihara element and to improve performance in axisymmetric problems [72, 73]. A similar method was developed in [65] to improve the bending solution of the Pian-Sumihara element on distorted meshes. Later, the penalty equilibrium formulation was applied to fracture mechanics [74] and extended to the Hu–Washizu variational principle [15, 16]. The addition of an equilibrium penalty term is also used in [12, 69] to construct superconvergent stress recovery methods.

We start with a modified Hellinger–Reissner functional with an equilibrium penalty term:

$$\begin{aligned} \Pi_{\text{HR}^*}[\mathbf{u}, \boldsymbol{\sigma}] = & -\frac{1}{2} \int_{\Omega} \boldsymbol{\sigma} : \mathbb{C}^{-1} : \boldsymbol{\sigma} \, d\mathbf{x} + \int_{\Omega} \boldsymbol{\sigma} : \nabla_s \mathbf{u} \, d\mathbf{x} - \int_{\Omega} \mathbf{b} \cdot \mathbf{u} \, d\mathbf{x} - \int_{\Gamma_t} \bar{\mathbf{t}} \cdot \mathbf{u} \, ds \\ & - \frac{\alpha}{2} \int_{\Omega} (\nabla \cdot \boldsymbol{\sigma} + \mathbf{b}) \cdot (\nabla \cdot \boldsymbol{\sigma} + \mathbf{b}) \, d\mathbf{x}, \end{aligned} \quad (23)$$

where $\alpha > 0$ is a penalty parameter. After taking the first variation, the stationary condition results in the weak equilibrium equations and modified strain-displacement relations:

$$\int_{\Omega} \boldsymbol{\sigma} : \nabla_s(\delta \mathbf{u}) \, d\mathbf{x} - \int_{\Omega} \mathbf{b} \cdot \delta \mathbf{u} \, d\mathbf{x} - \int_{\Gamma_t} \bar{\mathbf{t}} \cdot \delta \mathbf{u} \, ds = 0 \quad \forall \delta \mathbf{u} \in \mathcal{V}_u, \quad (24a)$$

$$\int_{\Omega} \delta \boldsymbol{\sigma} : (\nabla_s \mathbf{u} - \mathbb{C}^{-1} : \boldsymbol{\sigma}) \, d\mathbf{x} - \alpha \int_{\Omega} (\nabla \cdot \delta \boldsymbol{\sigma}) \cdot (\nabla \cdot \boldsymbol{\sigma} + \mathbf{b}) = 0 \quad \forall \delta \boldsymbol{\sigma} \in \mathcal{V}_{\sigma}. \quad (24b)$$

5.1. Penalized stress-hybrid projection

Using (24b) over each element E , we define a stress projection operator by the condition:

$$\int_E \mathbb{P} : (\nabla_s \mathbf{u} - \mathbb{C}^{-1} : \Pi_{\beta} \boldsymbol{\sigma}) \, d\mathbf{x} - \alpha \int_E (\nabla \cdot \mathbb{P}) \cdot (\nabla \cdot \Pi_{\beta} \boldsymbol{\sigma} + \mathbf{b}) \, d\mathbf{x} = 0,$$

which can be rewritten as

$$\int_E \mathbb{P} : \mathbb{C}^{-1} : \Pi_{\beta} \boldsymbol{\sigma} \, d\mathbf{x} + \alpha \int_E (\nabla \cdot \mathbb{P}) \cdot (\nabla \cdot \Pi_{\beta} \boldsymbol{\sigma}) \, d\mathbf{x} = \int_E \mathbb{P} : \nabla_s \mathbf{u} \, d\mathbf{x} - \alpha \int_E (\nabla \cdot \mathbb{P}) \cdot \mathbf{b} \, d\mathbf{x}.$$

After applying the divergence theorem, we get

$$\begin{aligned} & \int_E \mathbb{P} : \mathbb{C}^{-1} : \Pi_{\beta} \boldsymbol{\sigma} \, d\mathbf{x} + \alpha \int_E (\nabla \cdot \mathbb{P}) \cdot (\nabla \cdot \Pi_{\beta} \boldsymbol{\sigma}) \, d\mathbf{x} \\ & = \int_{\partial E} (\mathbb{P} \cdot \mathbf{n}) \cdot \mathbf{u} \, ds - \int_E (\nabla \cdot \mathbb{P}) \cdot \mathbf{u} \, d\mathbf{x} - \alpha \int_E (\nabla \cdot \mathbb{P}) \cdot \mathbf{b} \, d\mathbf{x}. \end{aligned} \quad (26)$$

Using Voigt notation, we rewrite (26) in terms of matrix-vector operations

$$\begin{aligned} \int_E \bar{\mathbb{P}}^T \mathbf{C}^{-1} \overline{\Pi_\beta \boldsymbol{\sigma}} \, d\mathbf{x} + \alpha \int_E (\boldsymbol{\partial} \bar{\mathbb{P}})^T \boldsymbol{\partial} \overline{\Pi_\beta \boldsymbol{\sigma}} \, d\mathbf{x} &= \int_{\partial E} \bar{\mathbb{P}}^T \mathbf{N}^{\partial E} \mathbf{u} \, ds - \int_E (\boldsymbol{\partial} \bar{\mathbb{P}})^T \mathbf{u} \, d\mathbf{x} \\ &- \alpha \int_E (\boldsymbol{\partial} \bar{\mathbb{P}})^T \mathbf{b} \, d\mathbf{x}. \end{aligned} \quad (27)$$

5.2. Implementation of penalized stress-hybrid projection

From (27), we have the discrete expression:

$$\begin{aligned} \int_E \bar{\mathbb{P}}^T \mathbf{C}^{-1} \overline{\Pi_\beta \boldsymbol{\sigma}} \, d\mathbf{x} + \alpha \int_E (\boldsymbol{\partial} \bar{\mathbb{P}})^T \boldsymbol{\partial} \overline{\Pi_\beta \boldsymbol{\sigma}} \, d\mathbf{x} &= \int_{\partial E} \bar{\mathbb{P}}^T \mathbf{N}^{\partial E} \mathbf{u}_h \, ds - \int_E (\boldsymbol{\partial} \bar{\mathbb{P}})^T \mathbf{u}_h \, d\mathbf{x} \\ &- \alpha \int_E (\boldsymbol{\partial} \bar{\mathbb{P}})^T \mathbf{b} \, d\mathbf{x}. \end{aligned} \quad (28a)$$

The second term on the right-hand side is not computable from the element DOF's; however, by applying the definition of the virtual element space (10), we rewrite the relation in a computable form

$$\begin{aligned} \int_E \bar{\mathbb{P}}^T \mathbf{C}^{-1} \overline{\Pi_\beta \boldsymbol{\sigma}} \, d\mathbf{x} + \alpha \int_E (\boldsymbol{\partial} \bar{\mathbb{P}})^T \boldsymbol{\partial} \overline{\Pi_\beta \boldsymbol{\sigma}} \, d\mathbf{x} &= \int_{\partial E} \bar{\mathbb{P}}^T \mathbf{N}^{\partial E} \mathbf{u}_h \, ds - \int_E (\boldsymbol{\partial} \bar{\mathbb{P}})^T \Pi^\varepsilon \mathbf{u}_h \, d\mathbf{x} \\ &- \alpha \int_E (\boldsymbol{\partial} \bar{\mathbb{P}})^T \mathbf{b} \, d\mathbf{x}. \end{aligned} \quad (28b)$$

Letting $\bar{\mathbb{P}} = \mathbf{P}$, $\overline{\Pi_\beta \boldsymbol{\sigma}} = \mathbf{P}\boldsymbol{\beta}$ and $\mathbf{u}_h = \boldsymbol{\varphi}\mathbf{d}$, we obtain the system of equations:

$$\begin{aligned} \left(\int_E \mathbf{P}^T \mathbf{C}^{-1} \mathbf{P} \, d\mathbf{x} + \alpha \int_E (\boldsymbol{\partial} \mathbf{P})^T \boldsymbol{\partial} \mathbf{P} \, d\mathbf{x} \right) \boldsymbol{\beta} \\ = \left(\int_{\partial E} \mathbf{P}^T \mathbf{N}^{\partial E} \boldsymbol{\varphi} \, ds - \int_E (\boldsymbol{\partial} \mathbf{P})^T \Pi^\varepsilon \boldsymbol{\varphi} \, d\mathbf{x} \right) \mathbf{d} - \alpha \int_E (\boldsymbol{\partial} \mathbf{P})^T \mathbf{b} \, d\mathbf{x}. \end{aligned} \quad (29)$$

Define the corresponding matrices by

$$\mathbf{H} = \int_E \mathbf{P}^T \mathbf{C}^{-1} \mathbf{P} \, d\mathbf{x}, \quad \mathbf{H}_p = \int_E (\boldsymbol{\partial} \mathbf{P})^T \boldsymbol{\partial} \mathbf{P} \, d\mathbf{x}, \quad (30a)$$

$$\mathbf{L} = \int_{\partial E} \mathbf{P}^T \mathbf{N}^{\partial E} \boldsymbol{\varphi} \, ds - \int_E (\boldsymbol{\partial} \mathbf{P})^T \Pi^\varepsilon \boldsymbol{\varphi} \, d\mathbf{x}, \quad \mathbf{L}_p = \int_E (\boldsymbol{\partial} \mathbf{P})^T \mathbf{b} \, d\mathbf{x}. \quad (30b)$$

Then the stress coefficients are given as

$$\boldsymbol{\beta} = (\mathbf{H} + \alpha \mathbf{H}_p)^{-1} (\mathbf{L}\mathbf{d} - \alpha \mathbf{L}_p). \quad (30c)$$

5.3. Element stiffness matrix and element force vector

To construct the element stiffness matrix, we first consider the discrete equilibrium equations based on (24a)

$$\int_E \overline{\Pi_\beta \boldsymbol{\sigma}(\mathbf{u}_h)}^T \nabla_s (\delta \mathbf{u}_h) \, d\mathbf{x} = \int_E \mathbf{b}^T \delta \mathbf{u}_h \, d\mathbf{x} + \int_{\Gamma_t} \bar{\mathbf{t}}^T \delta \mathbf{u}_h \, ds.$$

On applying (24b) and simplifying, we rewrite the first integral as

$$\begin{aligned} \int_E \overline{\Pi_\beta \boldsymbol{\sigma}(\mathbf{u}_h)}^T \nabla_s(\delta \mathbf{u}_h) d\mathbf{x} &= \int_E \overline{\Pi_\beta \boldsymbol{\sigma}(\mathbf{u}_h)}^T \mathbf{C}^{-1} \overline{\Pi_\beta \boldsymbol{\sigma}(\delta \mathbf{u}_h)} d\mathbf{x} \\ &+ \alpha \int_E (\partial \overline{\Pi_\beta \boldsymbol{\sigma}(\mathbf{u}_h)})^T (\partial \overline{\Pi_\beta \boldsymbol{\sigma}(\delta \mathbf{u}_h)} + \mathbf{b}) d\mathbf{x}. \end{aligned} \quad (31)$$

Now we have the equation

$$\begin{aligned} \int_E \overline{\Pi_\beta \boldsymbol{\sigma}(\mathbf{u}_h)}^T \mathbf{C}^{-1} \overline{\Pi_\beta \boldsymbol{\sigma}(\delta \mathbf{u}_h)} d\mathbf{x} &+ \alpha \int_E (\partial \overline{\Pi_\beta \boldsymbol{\sigma}(\mathbf{u}_h)})^T (\partial \overline{\Pi_\beta \boldsymbol{\sigma}(\delta \mathbf{u}_h)} + \mathbf{b}) d\mathbf{x} \\ &= \int_E \mathbf{b}^T \delta \mathbf{u}_h d\mathbf{x} + \int_{\Gamma_t \cap \partial E} \bar{\mathbf{t}}^T \delta \mathbf{u}_h ds. \end{aligned} \quad (32)$$

After expanding $\overline{\Pi_\beta \boldsymbol{\sigma}} = \mathbf{P}\boldsymbol{\beta}$ and simplifying, we construct the element stiffness matrix

$$\mathbf{K}_E = \mathbf{L}^T (\mathbf{H} + \alpha \mathbf{H}_p)^{-1} \mathbf{L}, \quad (33a)$$

and the element force vector is given by

$$\mathbf{f}_E = \int_E \boldsymbol{\varphi}^T \mathbf{b} d\mathbf{x} + \int_{\Gamma_t \cap \partial E} \boldsymbol{\varphi}^T \bar{\mathbf{t}} ds + \alpha \mathbf{L}^T (\mathbf{H} + \alpha \mathbf{H}_p)^{-1} \mathbf{L}_p, \quad (33b)$$

where \mathbf{H} , \mathbf{H}_p , \mathbf{L} , \mathbf{L}_p are given in (30).

5.4. Choice of penalty parameter and stress basis functions

Similar to the stabilized virtual element method, one drawback of the penalty equilibrium method is the need for a properly designed penalty parameter α . In [72], $\alpha = \frac{\kappa}{E_Y}$, where E_Y is the Young's modulus and $\kappa > 10^3$ is a large dimensionless number, is suggested. However, we found that this can result in the loss of stability for problems with highly distorted meshes. It is suggested in [16], that the penalty term should be scaled by a term that depends on the geometry in order to attain consistent units. In particular, α is chosen to be of the form $\alpha = \frac{\kappa \ell_0^2}{E_Y}$, where ℓ_0 is a characteristic length that is dependent on the element geometry. In our tests, we let ℓ_0 be the minimum length from the element centroid to the nodes and $\kappa = 10^4$. From our numerical experiments on benchmark problems, we found that using the penalty parameter $\alpha = \frac{\kappa \ell_0^2}{E_Y}$ resulted in higher accuracy and superconvergence on sufficiently refined uniform meshes. However, in the case when E_Y is small (α too large), low energy modes appear in the element stiffness matrix. From [44], it is suggested that a reasonable value of $\frac{\kappa}{E_Y}$ is between 10 and 100; therefore, we fix an arbitrary upper bound of 10 in our tests. That is, we use

$$\alpha = \min \left\{ 10, \frac{\kappa}{E_Y} \right\} \ell_0^2. \quad (34)$$

For the penalty equilibrium stress-hybrid method, we do not require the equilibrated stress basis functions given in (14). Instead, we seek the smallest number of stress basis functions that still retains stability and is not overly stiff in bending. For a six-noded element, a minimum of nine terms are needed; but it was found in [19] that the 9β complete

linear basis is not sufficient for stability. We choose the 12β expansion with complete bilinear polynomials given by

$$\mathbf{P} = \begin{bmatrix} 1 & 0 & 0 & \xi & 0 & 0 & \eta & 0 & 0 & \xi\eta & 0 & 0 \\ 0 & 1 & 0 & 0 & \xi & 0 & 0 & \eta & 0 & 0 & \xi\eta & 0 \\ 0 & 0 & 1 & 0 & 0 & \xi & 0 & 0 & \eta & 0 & 0 & \xi\eta \end{bmatrix}. \quad (35)$$

6. Numerical results

We present a series of numerical examples in linear elasticity under plane strain conditions on a variety of meshes. The unstructured triangular meshes used in these examples are generated using DistMesh [50]. We compute the errors of the displacement in the L^2 norm and energy seminorm, and the L^2 error of the hydrostatic stress (denoted by \tilde{p}). The convergence rates of CT FEM, B-bar VEM, SH-VEM, and PSH-VEM are computed using the following discrete error measures:

$$\|\mathbf{u} - \mathbf{u}_h\|_{L^2(\Omega)} = \sqrt{\sum_E \int_E |\mathbf{u} - \Pi^\varepsilon \mathbf{u}_h|^2 d\mathbf{x}}, \quad (36a)$$

$$\|\tilde{p} - \tilde{p}_h\|_{L^2(\Omega)} = \sqrt{\sum_E \int_E |\tilde{p} - \tilde{p}_h|^2 d\mathbf{x}}, \quad (36b)$$

$$\|\mathbf{u} - \mathbf{u}_h\|_a = \sqrt{\sum_E \int_E (\bar{\boldsymbol{\sigma}} - \overline{\Pi_\beta \boldsymbol{\sigma}})^T \mathbf{C}^{-1} (\bar{\boldsymbol{\sigma}} - \overline{\Pi_\beta \boldsymbol{\sigma}}) d\mathbf{x}}. \quad (36c)$$

We use the scaled boundary cubature (SBC) method [21] to compute the matrices \mathbf{H} in (19a), \mathbf{H}_p , \mathbf{L} and \mathbf{L}_p in (30), and the integrals appearing in (36). The matrices \mathbf{H} , \mathbf{H}_p and \mathbf{L} are integrals of polynomial functions and are exactly computed by the SBC method. The integrals in (36) are in general not integrals of polynomials but they can be computed to arbitrary accuracy with the SBC method.

6.1. Eigenvalue analysis

We examine the eigenvalues of the SH-VEM for general triangular elements to determine the stability of the method. The material has Young's modulus $E_Y = 1$ psi and Poisson's ratio $\nu = 0.49995$. We assess the eigenvalues of the standard VEM [7], B-bar VEM [49], composite triangle FEM [34] and the three formulations: a 11β and 15β that is based on the Airy stress function basis given in (14), and a 13β hybrid formulation given in (15). For a stable method, the element stiffness matrix should have three zero eigenvalues that correspond to the zero-energy modes and the next smallest eigenvalue should be positive and bounded away from zero. For this test, we construct six-noded triangular elements with vertices at $\{(-1, 0), (1, 0), (\gamma_1, \gamma_2)\}$, where $\gamma_1 \in [-10, 10]$, $\gamma_2 \in [0.05, 10]$, and then nodes are placed at the midpoints of each edge (see Figure 2). For each combination of γ_1 and γ_2 , we compute the first non-rigid body eigenvalue, which corresponds to the fourth smallest eigenvalue of the element stiffness matrix. The contour plots of the first non-rigid body eigenvalue are given in Figure 3. The plots show that the 11β formulation will develop spurious modes as the elements become highly distorted. The 15β SH-VEM and B-bar VEM

produced similar ranges for their eigenvalues and both do not produce any spurious zero-energy modes. The eigenvalue in the 13β formulation had a similar range to the standard VEM and further numerical tests show that the 13β formulation locks in the incompressible limit. Therefore both the 11β Airy stress and 13β hybrid formulations are not considered in the remaining examples. The 15β SH-VEM will be denoted as SH-VEM in the later examples.

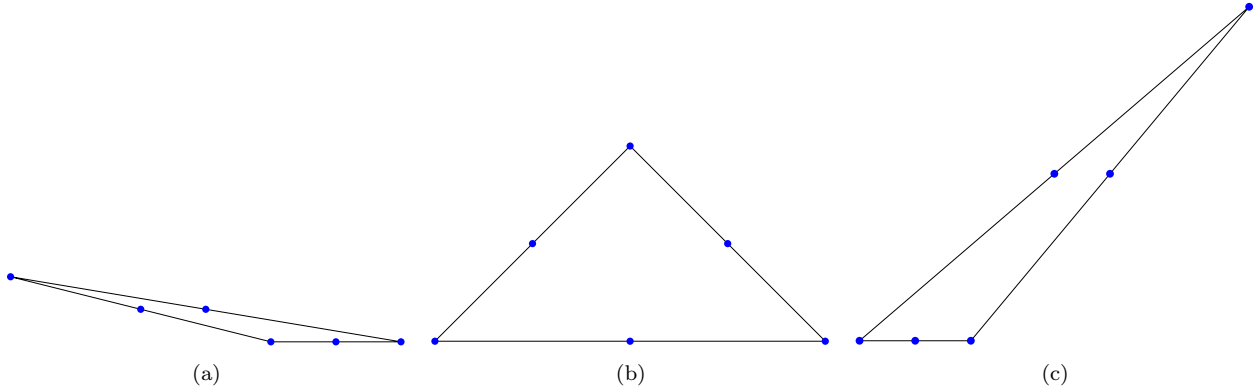


Figure 2: (a)-(c) Sequence of six-noded triangular elements with vertices at $\{(-1, 0), (1, 0), (\alpha, \beta)\}$ and nodes placed at the midpoint of each edge.

6.2. Eigenvalue analysis of the penalty formulation

We test the stability of the PSH-VEM with different values of the penalty parameter α . The material has Young's modulus $E_Y = 1$ psi and Poisson's ratio $\nu = 0.49995$. We choose four penalty parameters $\alpha \in \{\frac{\ell_0^2}{10}, \ell_0^2, 10\ell_0^2, 100\ell_0^2\}$ and examine the first non-rigid body eigenvalue of the element stiffness matrix of the penalty stress-hybrid formulation. For each α , we repeat the eigenvalue analysis presented in the previous section. In Figure 4, the contour plots of the the first non-rigid body eigenvalue as a function of (γ_1, γ_2) are shown. The plots reveal that as α increases, the maximum value of the eigenvalue decreases. This implies as $\alpha \rightarrow \infty$, the element stiffness matrix will be rank-deficient and lose stability. However, for the tested values of α , no spurious eigenvalues appear even for highly distorted elements.

6.3. Eigenvalue analysis for near incompressibility

It is known that in the incompressible limit ($\nu \rightarrow 0.5$) that the element stiffness matrix should only have one eigenvalue that tends to infinity [60]. Elements with more than one infinite eigenvalue will experience volumetric locking. We examine the eigenvalues of the element stiffness matrix for the standard VEM, CT FEM, B-bar VEM, 15β SH-VEM, and 12β PSH-VEM on a single element. The material has Young's modulus $E_Y = 1$ psi and Poisson's ratio $\nu = 0.4999999$. In Table 1, the five largest eigenvalues of each method is presented for a regular six-noded triangular element (see Figure 1c) and Table 2 shows the eigenvalues for a six-noded nonconvex element (see Figure 1a). The tables show that the standard virtual element approach has all five largest eigenvalues tending to infinity, which leads to severe volumetric locking. The composite element has three diverging eigenvalues,

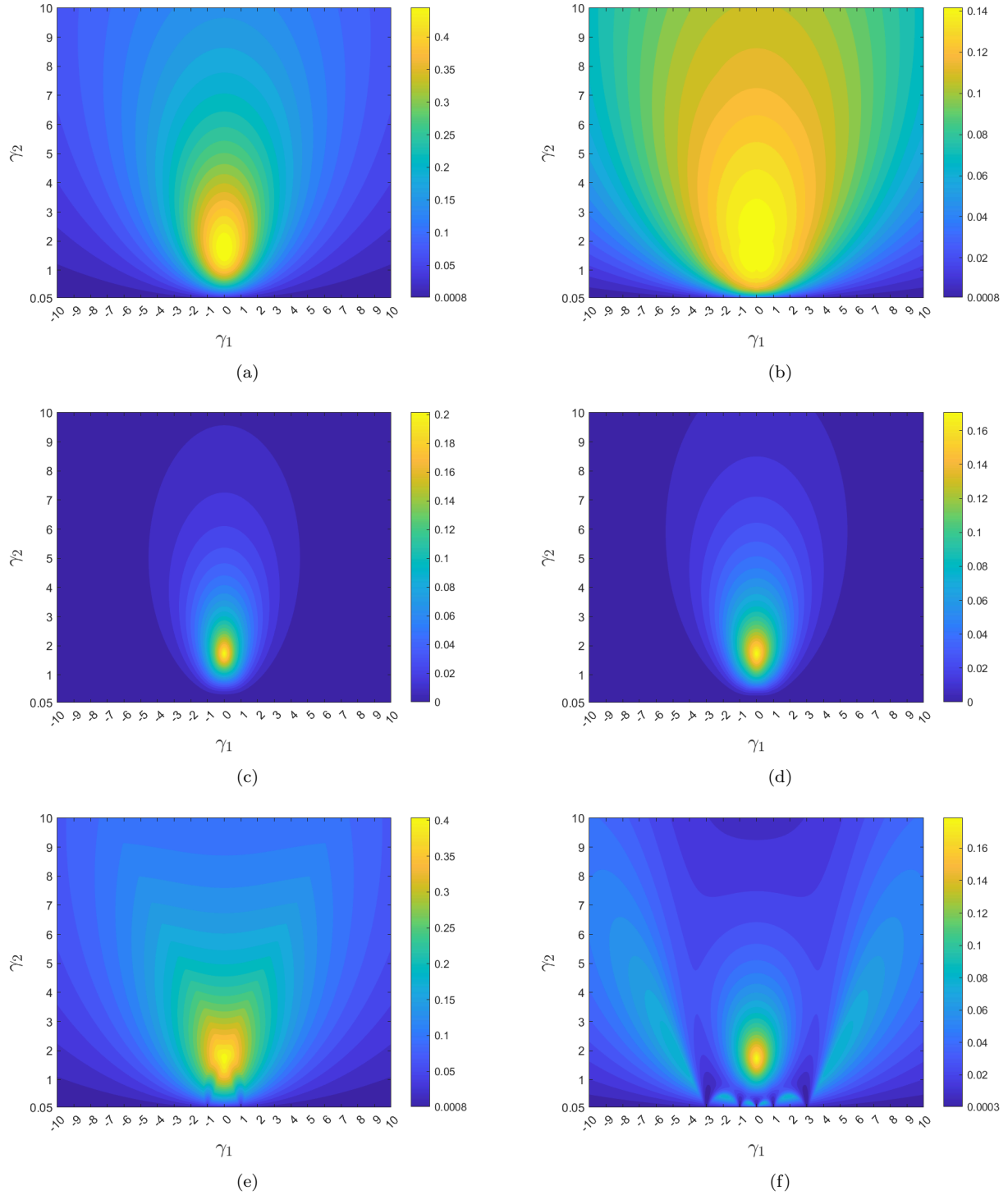


Figure 3: Contour plots of the fourth-lowest eigenvalue as a function of (γ_1, γ_2) for (a) standard VEM, (b) B-bar VEM, (c) CT FEM, (d) 11β SH-VEM, (e) 13β SH-VEM, and (f) 15β SH-VEM.

which can result in the mild locking behavior. The B-bar VEM, SH-VEM, and PSH-VEM have only a single large eigenvalue for both the regular and the nonconvex element.

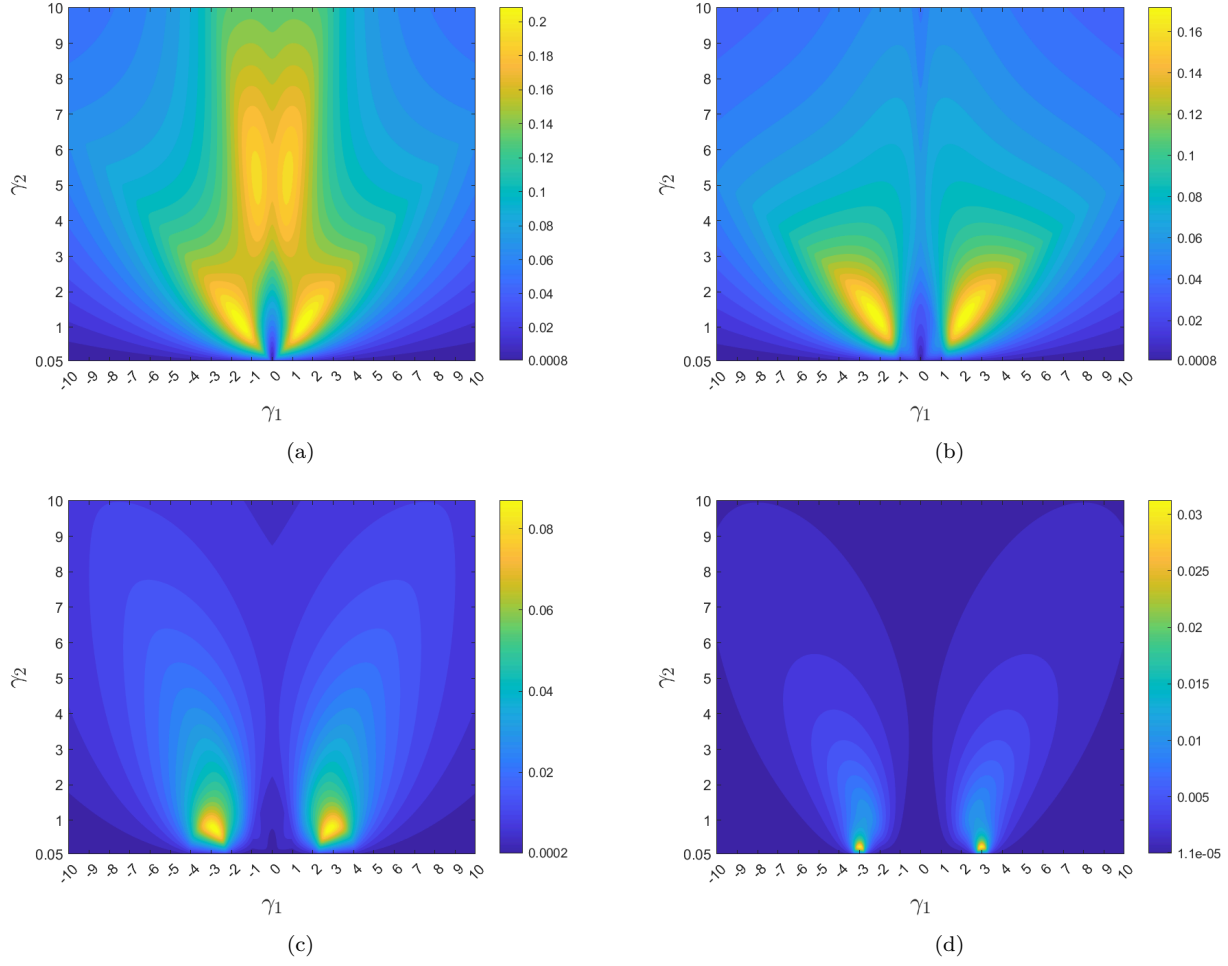


Figure 4: Contour plots of the fourth smallest eigenvalue as a function of (γ_1, γ_2) using the penalty parameters (a) $\alpha = \frac{\ell_0^2}{10}$, (b) $\alpha = \ell_0^2$, (c) $\alpha = 10\ell_0^2$, and (d) $\alpha = 100\ell_0^2$.

VEM	CT FEM	B-bar VEM	15β SH-VEM	12β PSH-VEM
1.1×10^6	8.1×10^{-1}	2.1×10^{-1}	6.3×10^{-1}	4.3×10^{-1}
1.2×10^6	1.2×10^0	2.2×10^{-1}	8.8×10^{-1}	8.2×10^{-1}
1.7×10^6	3.7×10^5	7.5×10^{-1}	1.9×10^0	8.4×10^{-1}
1.8×10^6	4.2×10^5	9.6×10^{-1}	4.5×10^1	2.8×10^0
5.0×10^6	4.6×10^5	4.2×10^6	4.2×10^6	4.2×10^6

Table 1: Comparison of the five largest eigenvalues of the element stiffness matrix on a six-noded triangular element.

6.4. Thin cantilever beam

We consider the problem of a thin cantilever beam subjected to a shear end load [67]. The material has Young's modulus $E_Y = 1 \times 10^5$ psi and Poisson's ratio $\nu = 0.49995$. The beam has a length of $L = 32$ inch, a height of $D = 1$ inch and a unit thickness. A fixed displacement is applied on the left boundary, while a shear end load of $P = -100$ lbf is applied on the right boundary. We first use a set of unstructured triangular meshes.

VEM	CT FEM	B-bar VEM	15β SH-VEM	12β PSH-VEM
1.2×10^6	5.8×10^{-1}	2.9×10^{-1}	5.3×10^{-1}	3.6×10^{-1}
1.3×10^6	1.9×10^0	3.9×10^{-1}	1.5×10^0	1.3×10^0
5.8×10^6	4.8×10^5	2.1×10^0	6.6×10^0	2.0×10^0
5.9×10^6	5.6×10^5	2.2×10^0	1.8×10^1	5.1×10^0
1.2×10^7	6.8×10^6	6.7×10^6	6.7×10^6	6.7×10^6

Table 2: Comparison of the five largest eigenvalues of the element stiffness matrix on a six-noded nonconvex element.

In Figure 5, we show examples of the unstructured meshes and in Figure 6 we show the convergence of the four methods in the displacement L^2 norm, energy seminorm, and L^2 norm of hydrostatic stress. Figure 7 shows the convergence of the end displacement and the contour plot of hydrostatic stress for the SH-VEM. For methods that experience volumetric locking, non-physical oscillations will appear in the hydrostatic stress field. The plots reveal that the two stress-hybrid approaches yield better results, with the PSH-VEM having superior convergence and accuracy in the displacement, energy, and hydrostatic stress.

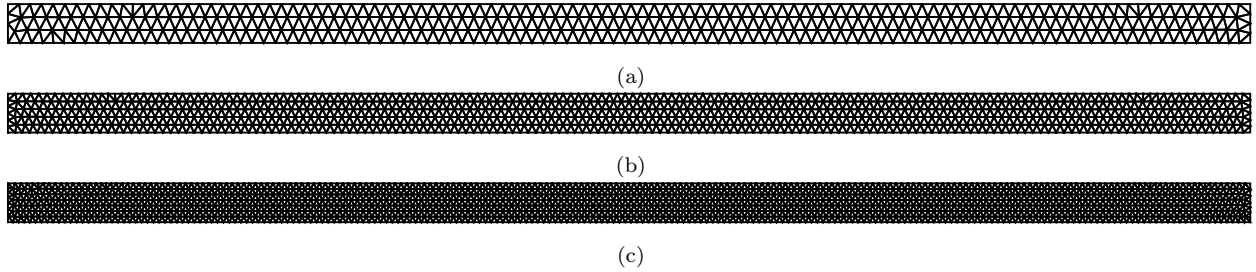


Figure 5: Unstructured triangular meshes for the cantilever beam problem. (a) 600 elements, (b) 1600 elements, and (c) 3000 elements.

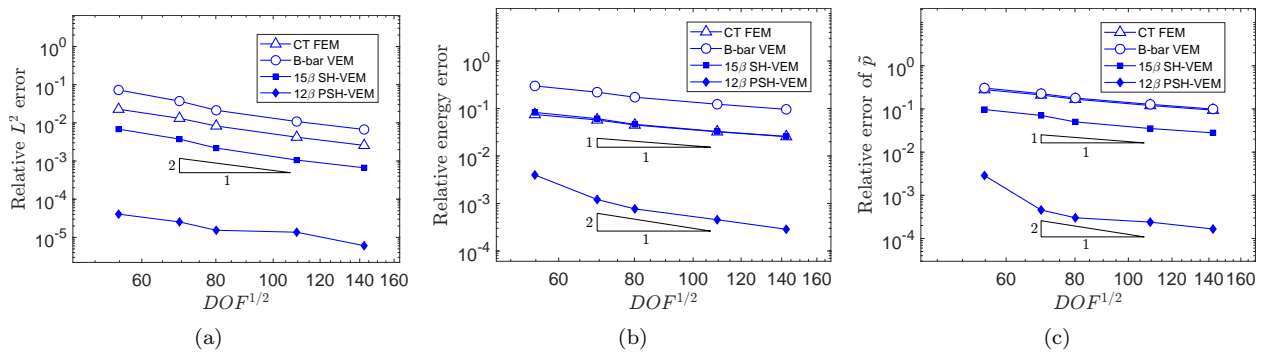


Figure 6: Comparison of CT FEM, B-bar VEM, SH-VEM and PSH-VEM for the thin cantilever beam problem on unstructured meshes. (a) L^2 error of displacement, (b) energy error, and (c) L^2 error of hydrostatic stress.

In the following tests, we examine the four methods on meshes with $N = 1$ and $N = 2$ elements along the height of the beam. For many formulations, these meshes will lead to overly stiff displacements and shear locking. The first set of meshes is constructed by taking a

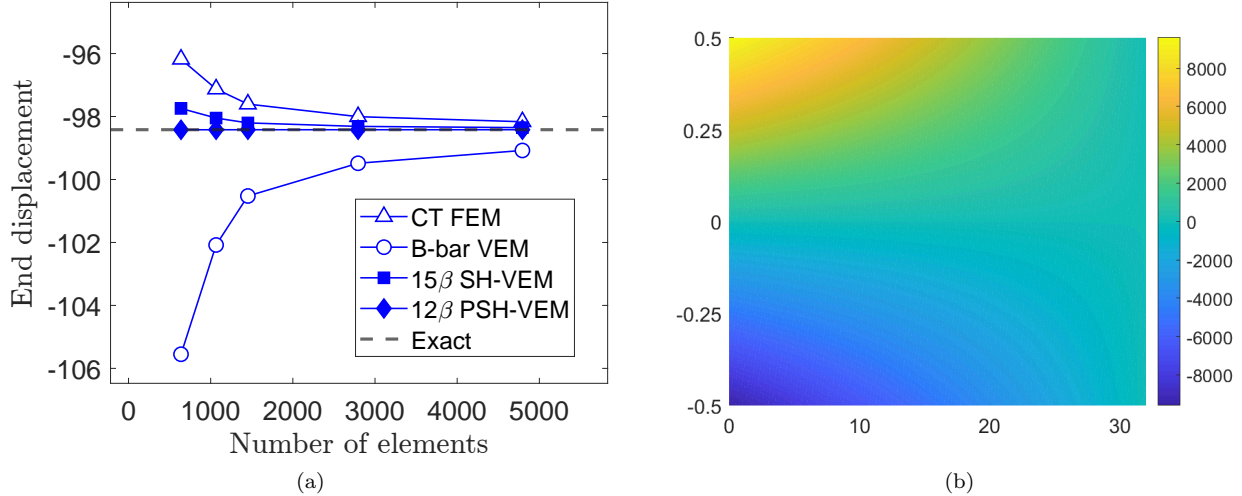


Figure 7: (a) Convergence of the end displacement for the cantilever beam problem. The mesh consists of unstructured triangles. (b) Contour plot of the hydrostatic stress for PSH-VEM.

uniform quadrilateral mesh and splitting each element into two right triangles (see Figure 8). The convergence of the end displacement of the four methods is presented in Figure 9. For $N = 1$, the two stress-hybrid methods are converging to the exact solution, while CT FEM experiences shear locking and B-bar VEM diverges from the exact solution (see Figure 9a) and for $N = 2$, B-bar VEM is still overly flexible (see Figure 9b). In both cases, the PSH-VEM shows far superior accuracy in displacement even on coarse meshes.

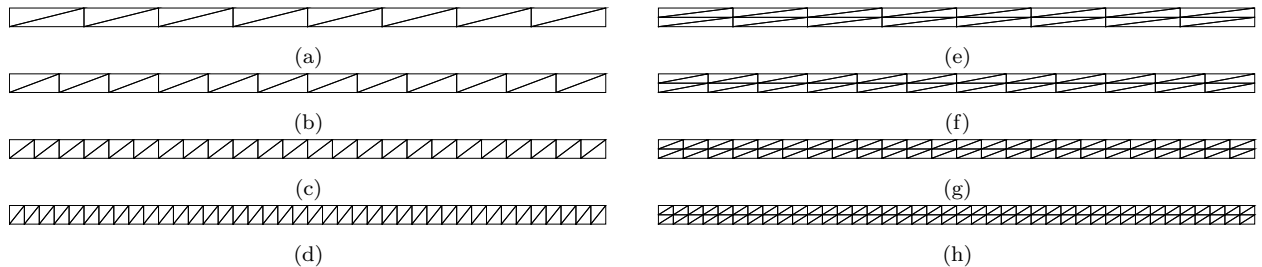


Figure 8: Structured meshes for the cantilever beam problem. Mesh is refined along the length with (a)-(d) 1 element along the height and (e)-(h) 2 elements along the height.

The second set of meshes is constructed by taking a uniform quadrilateral mesh and splitting each element along the two diagonals to form four triangles. The meshes are shown in Figure 10 and the convergence of the end displacement is depicted in Figure 11. The plots show that SH-VEM and PSH-VEM converge to the exact solution for both $N = 1$ and $N = 2$; however, the SH-VEM is much stiffer and less accurate than the penalty approach. CT FEM suffers from locking, while B-bar fails to converge for the case of a single element along the height.

The third set of meshes is constructed by taking the previous mesh and collapsing one of the triangles to a nearly degenerate triangle (see Figure 12). The plots showing the convergence of the end displacement is given in Figure 13. The plots reveal that for these meshes, the stress-hybrid methods are converging to the exact solution, while CT FEM and

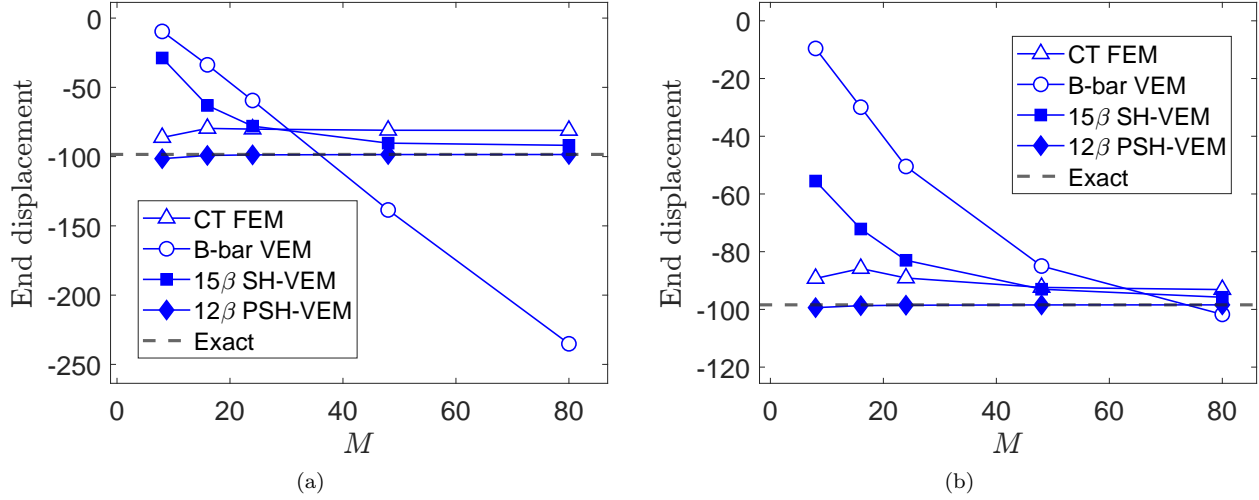


Figure 9: Convergence of the end displacement for the cantilever beam problem. The mesh consists of $M \times N$ right triangles, where M is the number of elements along the length of the beam. (a) $N = 1$ and (b) $N = 2$.

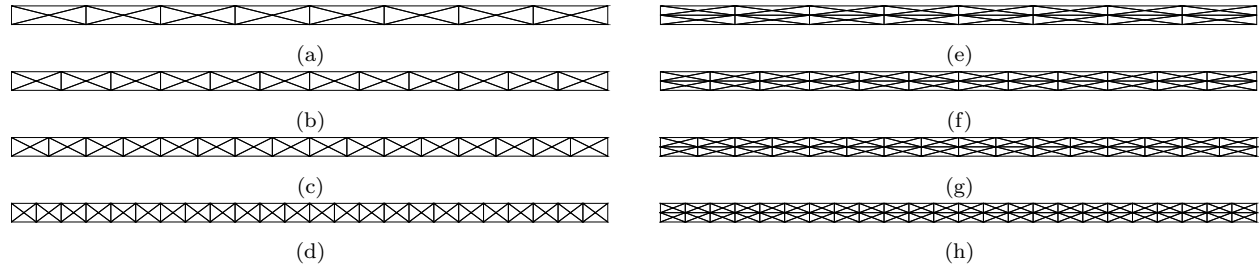


Figure 10: Structured meshes for the cantilever beam problem. Mesh is refined along the length with (a)-(d) 1 element along the height and (e)-(h) 2 elements along the height.

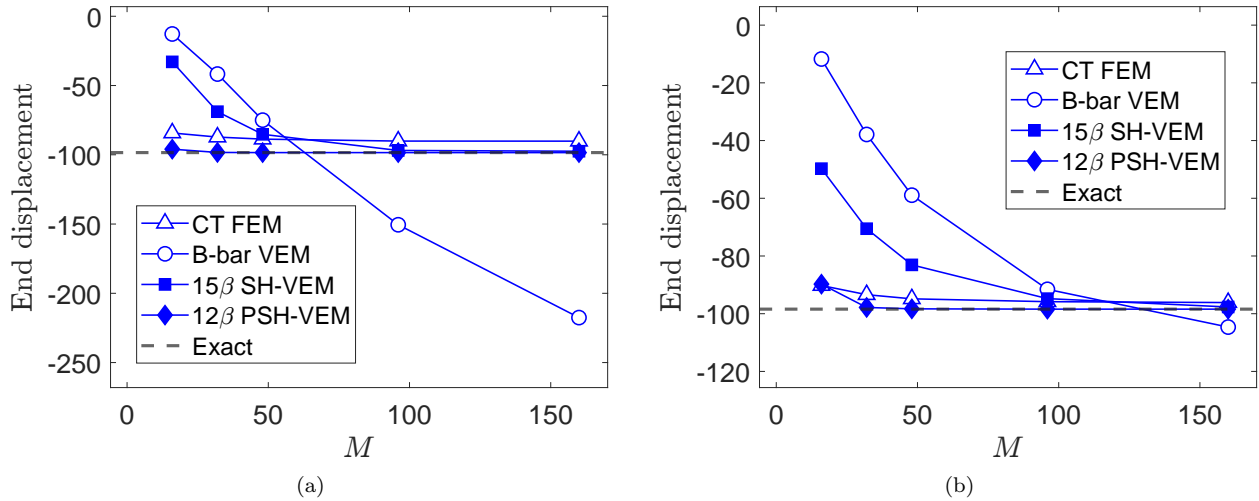


Figure 11: Convergence of the end displacement for the cantilever beam problem. The mesh consists of $M \times N$ triangles, where M is the number of elements along the length of the beam. (a) $N = 1$ and (b) $N = 2$.

B-bar VEM do not converge in the case of a single element along the height. When using two

elements along the height, the B-bar formulation is tending to the exact solution but is not accurate, while CT FEM still suffers from locking and does not converge. The PSH-VEM again attains a much more accurate solution than the other methods; however, it appears to be stiff for the coarsest mesh when $N = 2$.

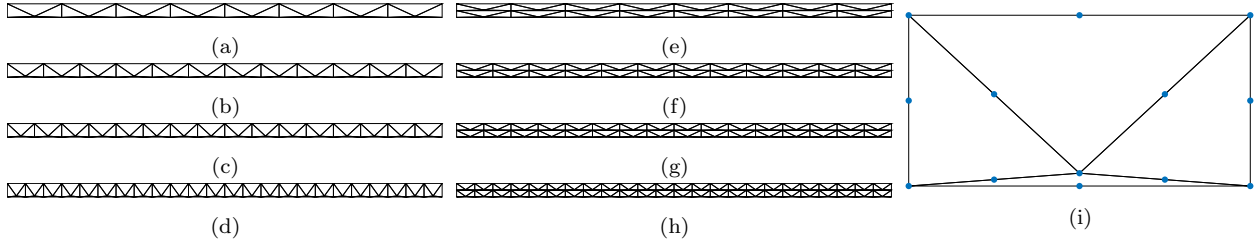


Figure 12: Structured nearly degenerate meshes for the cantilever beam problem. Mesh is refined along the length with (a)-(d) 1 element along the height and (e)-(h) 2 elements along the height. (i) Magnification of a single element split into four six-noded triangles.

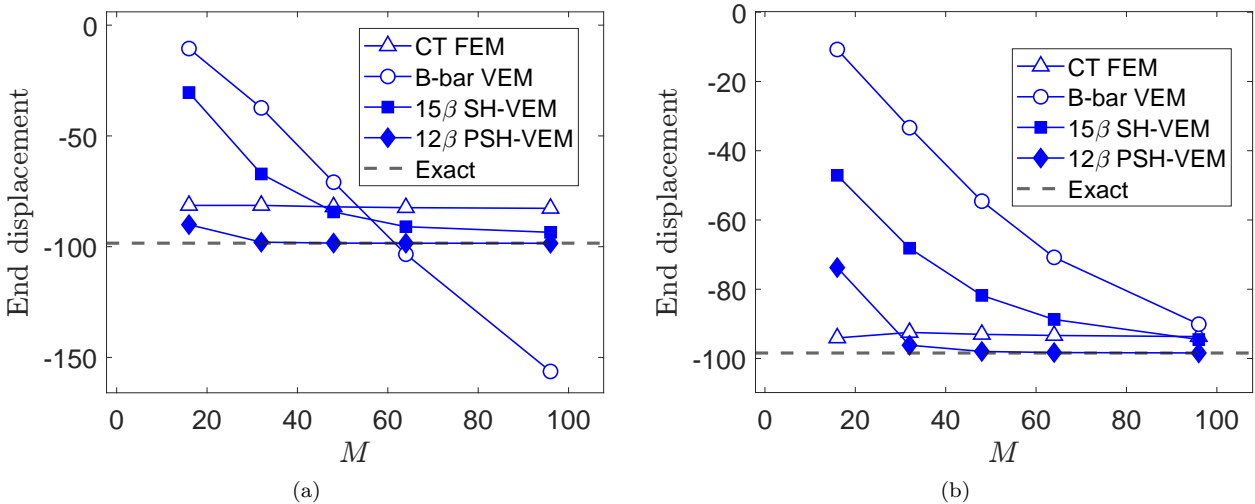


Figure 13: Convergence of the end displacement for the cantilever beam problem. The mesh consists of $M \times N$ triangles with some nearly degenerate, where M is the number of elements along the length of the beam. (a) $N = 1$ and (b) $N = 2$.

One benefit of the virtual element formulation is that it allows for very general element shapes. In particular, for the final set of meshes we use a mixture of distorted nonconvex hexagons and convex hexagons. A few representative meshes are shown in Figure 14. In Figure 15, we present the convergence of the end displacement for the four methods. In both cases $N = 1$ and $N = 2$, SH-VEM and PSH-VEM are convergent, but CT FEM is overly stiff.

Remark 3. The solutions produced by 15β SH-VEM are much stiffer than those found using the 5β formulation on quadrilaterals in [20]. In particular, for uniform rectangular meshes with $N = 1$, the 5β SH-VEM converges to nearly the exact solution with just $M = 8$ elements along the length of the beam. However, the PSH-VEM offers coarse mesh accuracy that is similar to the 5β SH-VEM.

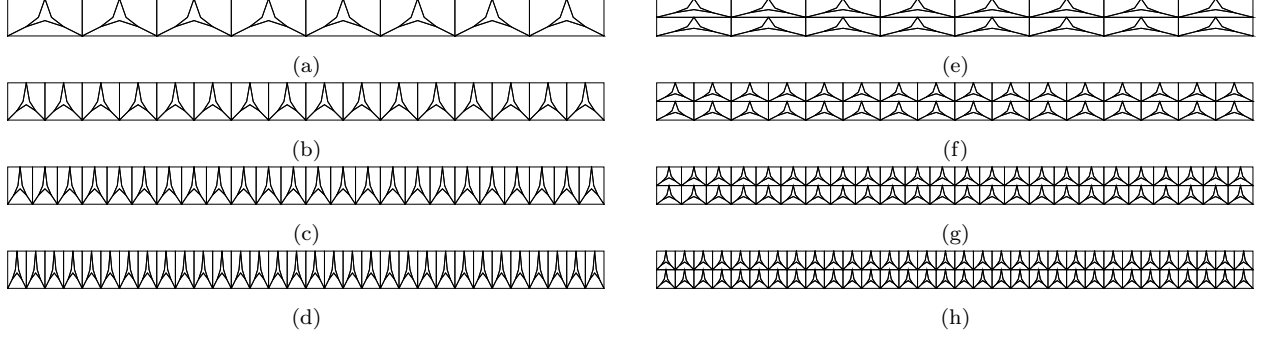


Figure 14: Meshes with nonconvex elements for the cantilever beam problem. Mesh is refined along the length with (a)-(d) 1 element along the height and (e)-(h) 2 elements along the height.

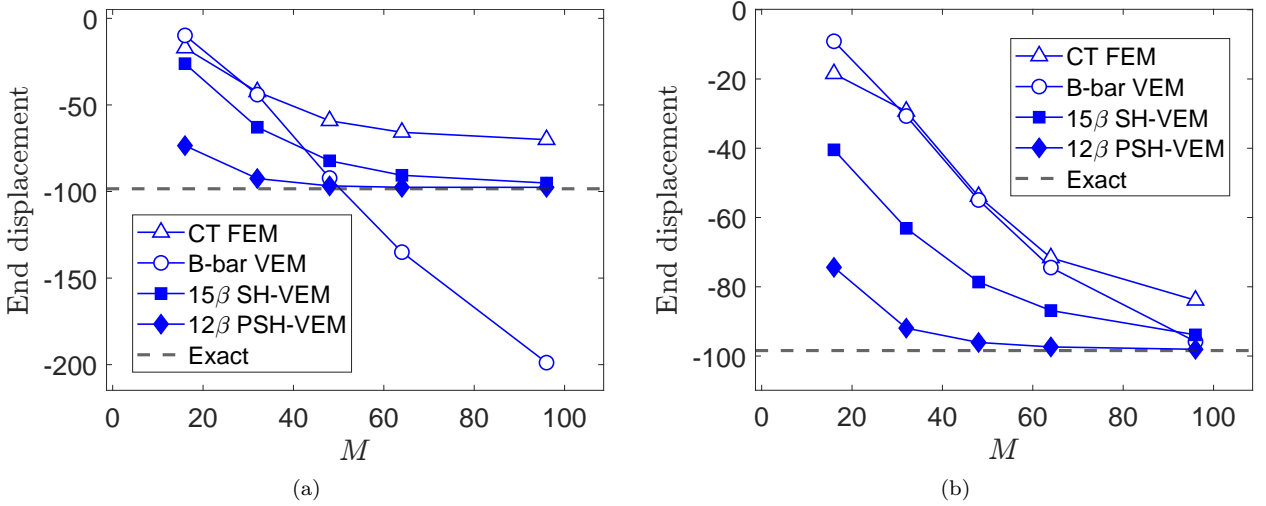


Figure 15: Convergence of the end displacement for the cantilever beam problem. The mesh consists of $M \times N$ convex and nonconvex elements, where M is the number of elements along the length of the beam. (a) $N = 1$ and (b) $N = 2$.

The penalty stress-hybrid approach provides the best accuracy for the cantilever beam problem; however, it relies on the choice of a suitable penalty parameter α . Therefore, we examine the sensitivity of the bending solution of PSH-VEM to the penalty parameter. For this test, we use the same material properties $E_Y = 1 \times 10^5$ psi and $\nu = 0.49995$. The problem is solved on a mesh consisting of $M \times 1$ right triangles (see Figure 8). The default penalty parameter is given by $\alpha = \frac{10^4 \ell_0^2}{E_Y} = 10^{-1} \ell_0^2$. To test the sensitivity of the parameter, we vary the penalty parameter three orders of magnitude on each side. That is, α is varied from $10^{-4} \ell_0^2$ to $10^2 \ell_0^2$. In Figure 16, the convergence of the end displacements for different values of α is presented. The plot shows that increasing α above the value $10^{-1} \ell_0^2$ does not greatly affect the solution; however, decreasing α makes the solution stiffer. If we decrease the value of α by three orders of magnitude to $\alpha = 10^{-4} \ell_0^2$, the solution becomes overly stiff and produces much larger errors than the other values of α .

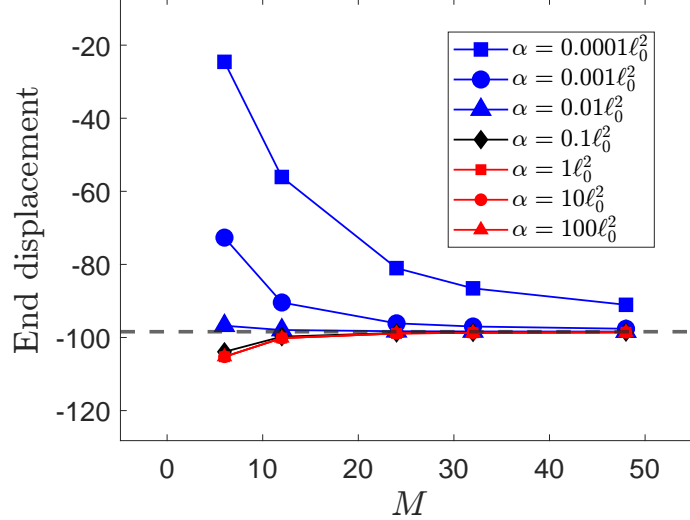


Figure 16: Comparison of the convergence of end displacement for PSH-VEM when using different choices of penalty parameter α . The mesh consists of $M \times 1$ right triangles, where M is the number of elements along the length of the beam.

6.5. Cook's membrane

Next, we consider the problem of the Cook's membrane under shear load [22]. This problem is commonly used to test the combined bending and shearing capabilities of an element. The material has Young's modulus $E_Y = 250$ psi and Poisson's ratio $\nu = 0.49995$. The left boundary of the membrane is clamped and a shear load of $F = 6.25$ lbf per unit length is applied along the right edge. The first set of meshes comprise of structured triangular meshes; a few sample meshes are shown in Figure 17. Figure 18 presents the convergence of the tip displacement of the four methods and the hydrostatic stress of the PSH-VEM. The plot in Figure 18a shows that, unlike in the cantilever beam problem, the CT FEM, SH-VEM, and PSH-VEM all perform worse than the B-bar formulation. Figure 18b shows that the PSH-VEM is able to produce a relatively smooth hydrostatic stress field with no visible signs of volumetric locking.

The second set of meshes that we test consists of unstructured triangles. In Figure 19, sample meshes are shown. The convergence of tip displacement and the contour plot of PSH-VEM is given in Figure 20. The plots show that for the unstructured mesh, SH-VEM and PSH-VEM have the fastest convergence, while B-Bar VEM becomes very flexible and converges from above. The hydrostatic stress contours of PSH-VEM remain smooth and agree with the contours found on structured meshes.

6.6. Plate with a circular hole

We consider the problem of an infinite plate with a circular hole of radius $a = 1$ inch under uniform tension [67]. The hole is assumed to be traction-free and a far-field load $\sigma_0 = 1$ psi is applied in the x -direction. Since the plate is symmetric, we model the problem as a quarter plate with length $L = 5$ inch and apply exact tractions along the boundary. The material has Young's modulus $E_Y = 2 \times 10^7$ psi and Poisson's ratio $\nu = 0.49995$. The first test of this problem is on unstructured triangular meshes with representative meshes shown in Figure 21. In Figure 22, we show the convergence results of the four methods

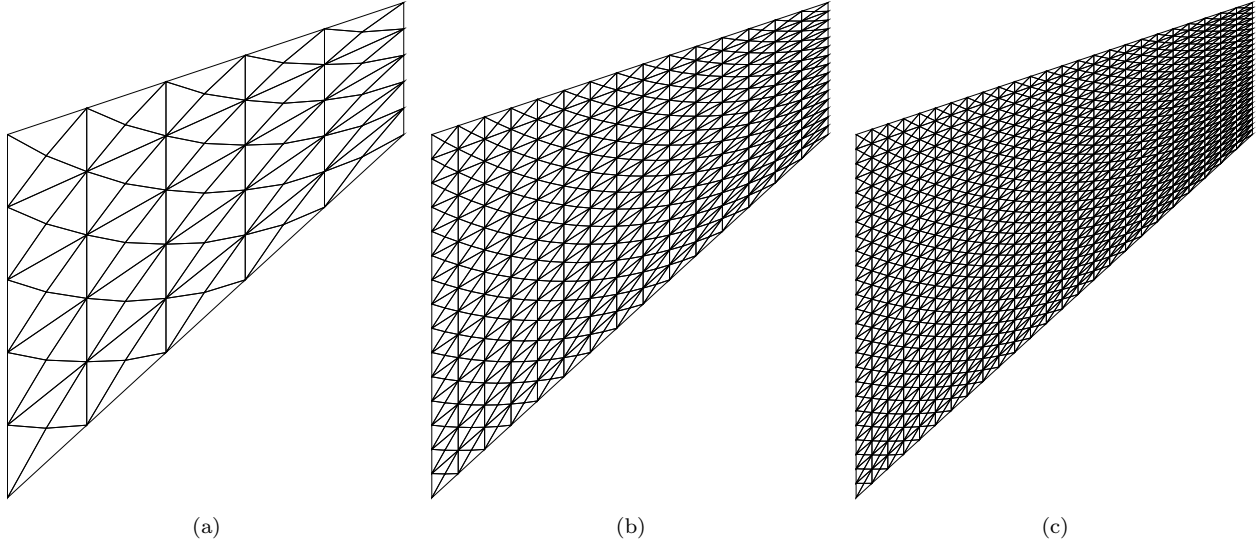


Figure 17: Structured triangular meshes for the Cook's membrane problem. (a) 100 elements, (b) 1000 elements, and (c) 2500 elements.

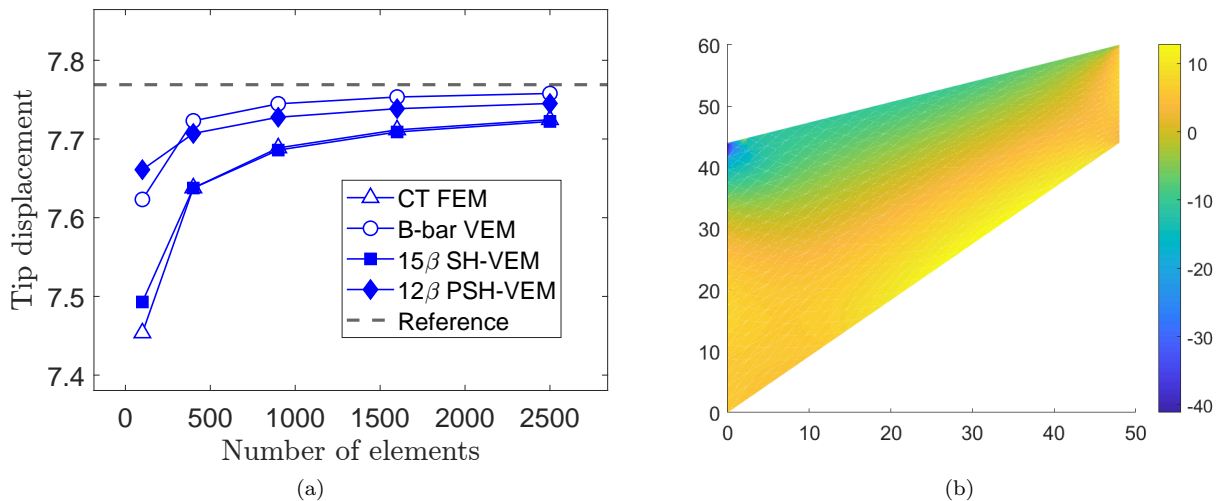


Figure 18: (a) Convergence of the tip displacement for Cook's membrane problem. The mesh consists of structured triangles. (b) Contour plot of the hydrostatic stress for PSH-VEM.

that are tested and find that the three methods CT FEM, B-bar VEM, and SH-VEM all have optimal convergence rates. However, the penalty stress-hybrid method has third order superconvergence in the energy seminorm and L^2 norm of hydrostatic stress. In Figure 23, we plot the contours of the pointwise error $\tilde{p} - \tilde{p}_h$ of the hydrostatic stress. The plots reveal that the penalty stress-hybrid method has the smallest pointwise error and the remaining three methods produce similar error distributions.

We now solve the problem on perturbed meshes. In [1], it is shown that small perturbations of a regular triangular mesh can lead to locking and a reduction in the rate of convergence in the hydrostatic stress error. For this test, we start with a regular quadrilateral mesh and then cut along both diagonals to create four triangles. The point of intersection of the two diagonals are perturbed for each quadrilateral. Representative meshes are shown

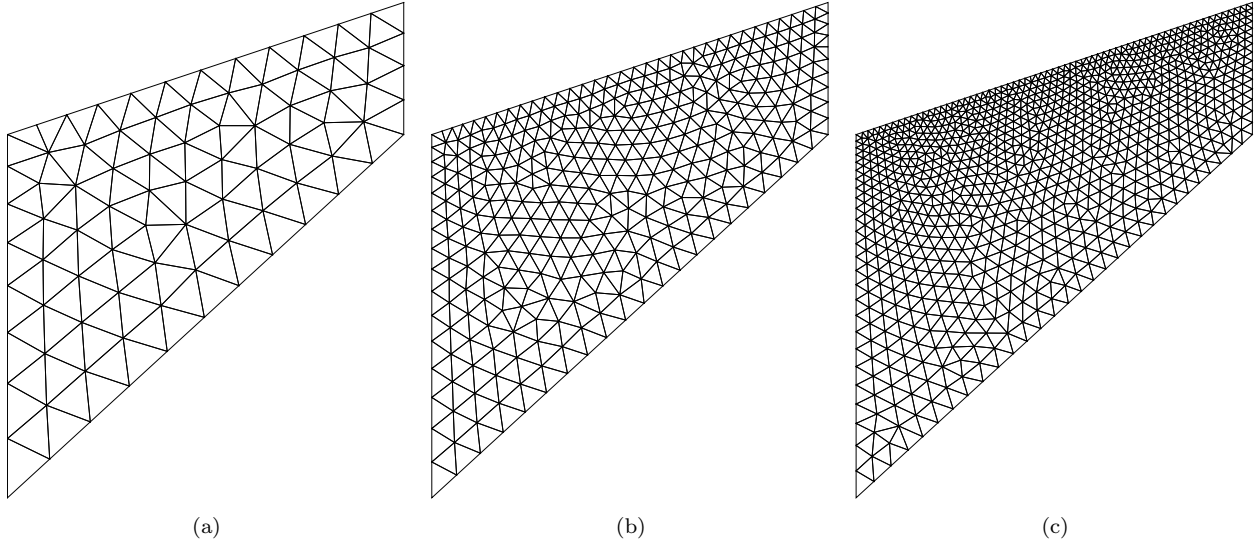


Figure 19: Unstructured triangular meshes for the Cook's membrane problem. (a) 100 elements, (b) 700 elements, and (c) 2000 elements.

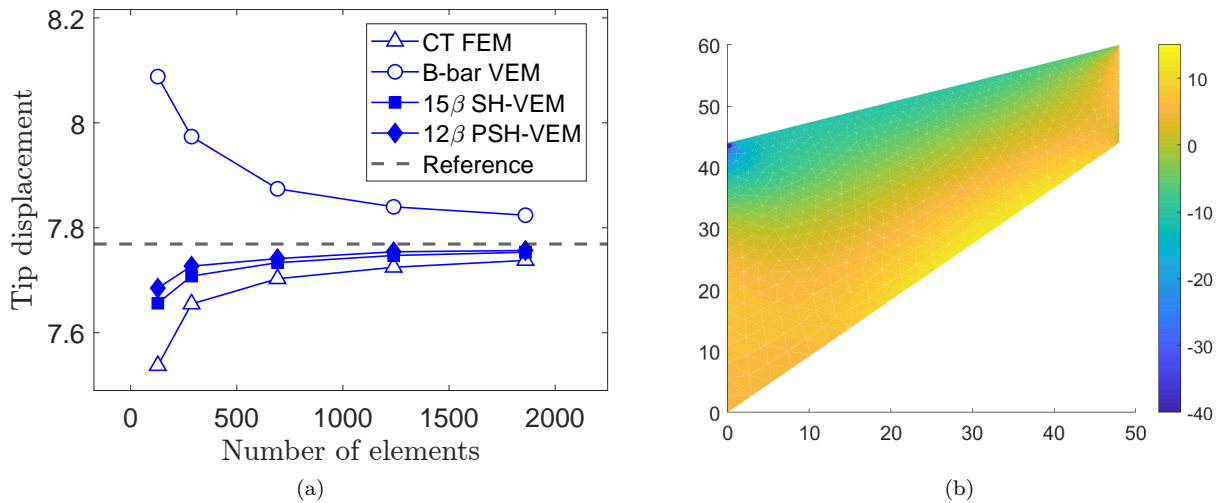


Figure 20: (a) Convergence of the tip displacement for Cook's membrane problem. The mesh consists of unstructured triangles. (b) Contour plot of the hydrostatic stress for PSH-VEM.

in Figure 24. In Figure 25, we plot the convergence of the four methods and find that CT FEM, B-bar VEM, and SH-VEM all still retain optimal rates of convergence. The penalty formulation exhibits second order superconvergence in the energy seminorm and L^2 norm of the hydrostatic stress. The contour plots in Figure 26 show that the four methods all have relatively smooth error distributions of the hydrostatic stress and display no signs of volumetric locking.

6.7. Hollow cylinder under internal pressure

Next, we consider a hollow cylinder subject to internal pressure [67]. By symmetry, the problem is modeled by a quarter cylinder with an outer radius $b = 5$ inch and an inner radius $a = 1$ inch. The outer radius of the cylinder is assumed to be traction-free, while a

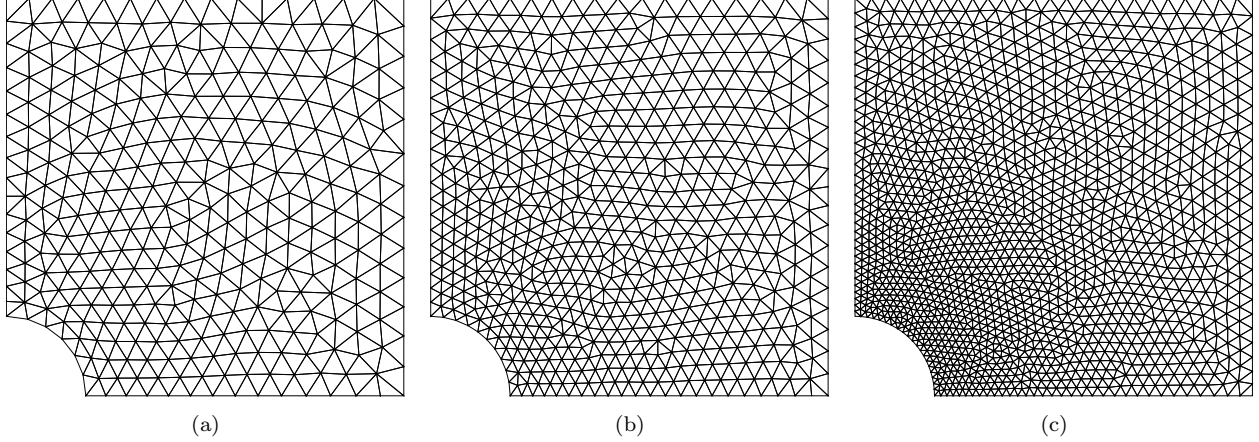


Figure 21: Unstructured triangular meshes for the plate with a hole problem. (a) 500 elements, (b) 1000 elements, and (c) 3000 elements.

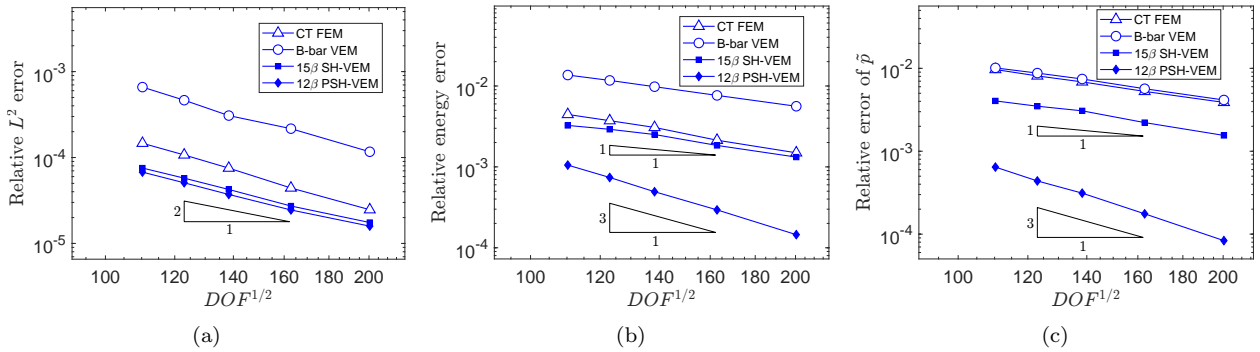


Figure 22: Comparison of CT FEM, B-bar VEM, SH-VEM, and PSH-VEM for the plate with a hole problem on unstructured meshes. (a) L^2 error of displacement, (b) energy error, and (c) L^2 error of hydrostatic stress.

uniform pressure of $p = 10^5$ psi is applied on the inner radius. The material properties are $E_Y = 2 \times 10^5$ psi and $\nu = 0.49995$. For this problem, the hydrostatic stress field is constant and we found that using nonconstant stress functions in the SH-VEM resulted in larger errors around the element corners. Therefore, we use an element averaged hydrostatic stress approximation for SH-VEM. We first solve the problem on structured triangular meshes; a few representative meshes are shown in Figure 27. In Figure 28, we show the rates of convergence in three error norms. The three methods CT FEM, B-bar VEM, and SH-VEM produce optimal convergence in the displacement L^2 norm, L^2 norm of hydrostatic stress as well as in the energy seminorm; while the PSH-VEM has second order superconvergence in the energy seminorm and third order in the L^2 norm of the hydrostatic stress. In Figure 29, we plot the contours of the relative error in the hydrostatic stress field for the four methods. The plots show that the maximum errors concentrate along the inner radius and improves when away from the boundary. The SH-VEM and PSH-VEM produce the smallest relative errors, with a maximum of around 8 and 1.2 percent, respectively.

We now test the hollow cylinder problem on an unstructured triangular mesh; a few representative meshes are presented in Figure 30. In Figure 31, the convergence results are given and again show that CT FEM, B-bar VEM, and SH-VEM deliver optimal rates. The

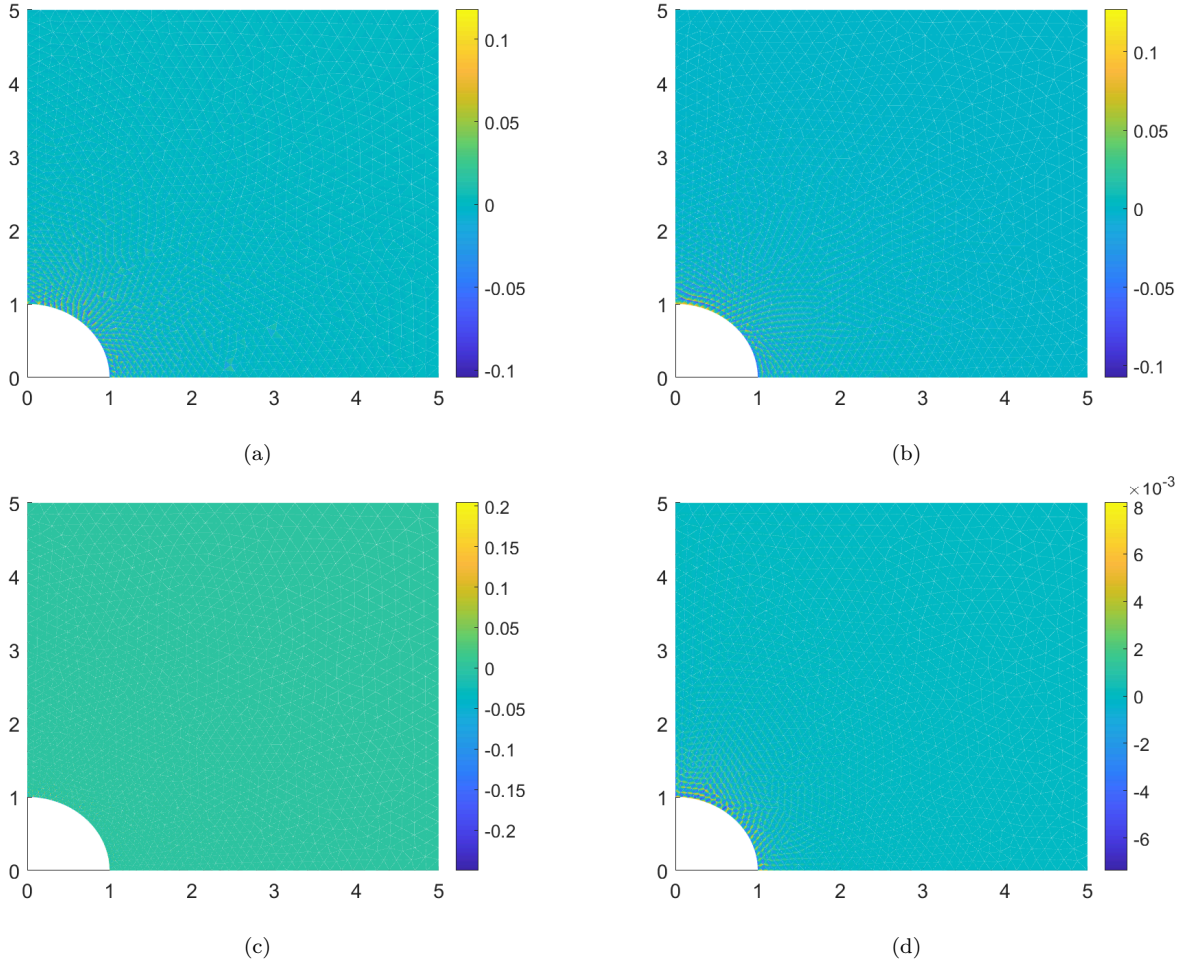


Figure 23: Contour plots of the error $\tilde{p} - \tilde{p}_h$ in hydrostatic stress on unstructured meshes for the plate with a circular hole problem. (a) CT FEM, (b) B-bar VEM, (c) SH-VEM, and (d) PSH-VEM.

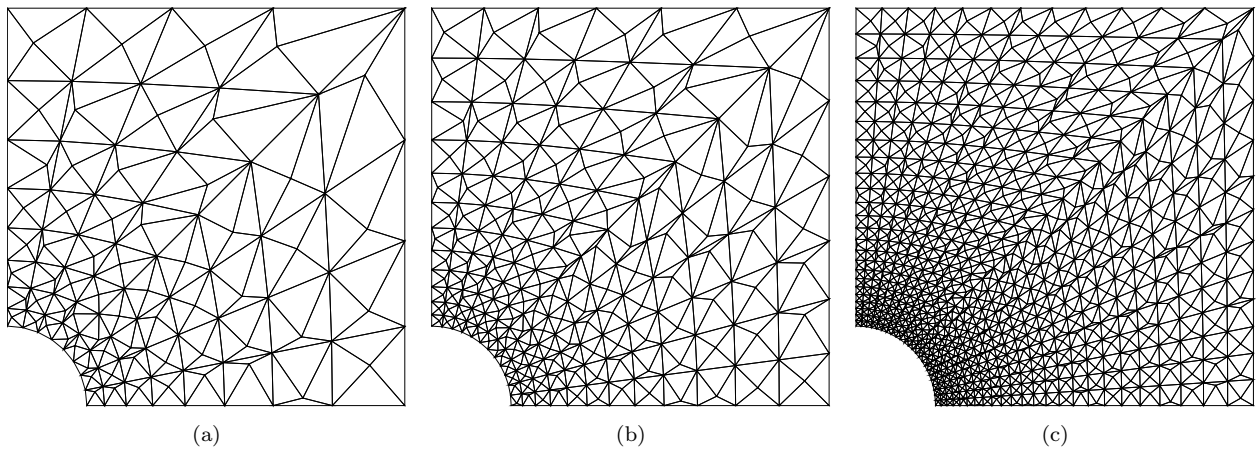


Figure 24: Perturbed triangular meshes for the plate with a hole problem. (a) 250 elements, (b) 500 elements, and (c) 2500 elements.

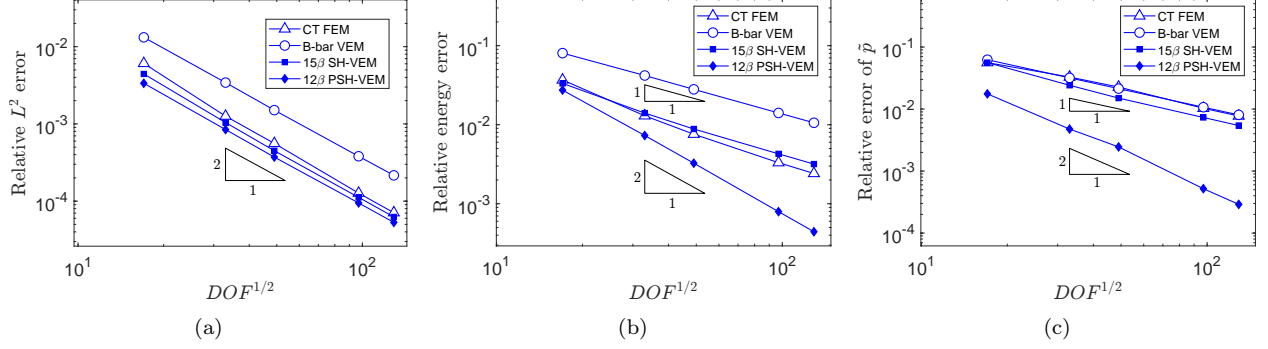


Figure 25: Comparison of CT FEM, B-bar VEM, SH-VEM, and PSH-VEM for the plate with a hole problem on perturbed meshes. (a) L^2 error of displacement, (b) energy error, and (c) L^2 error of hydrostatic stress.

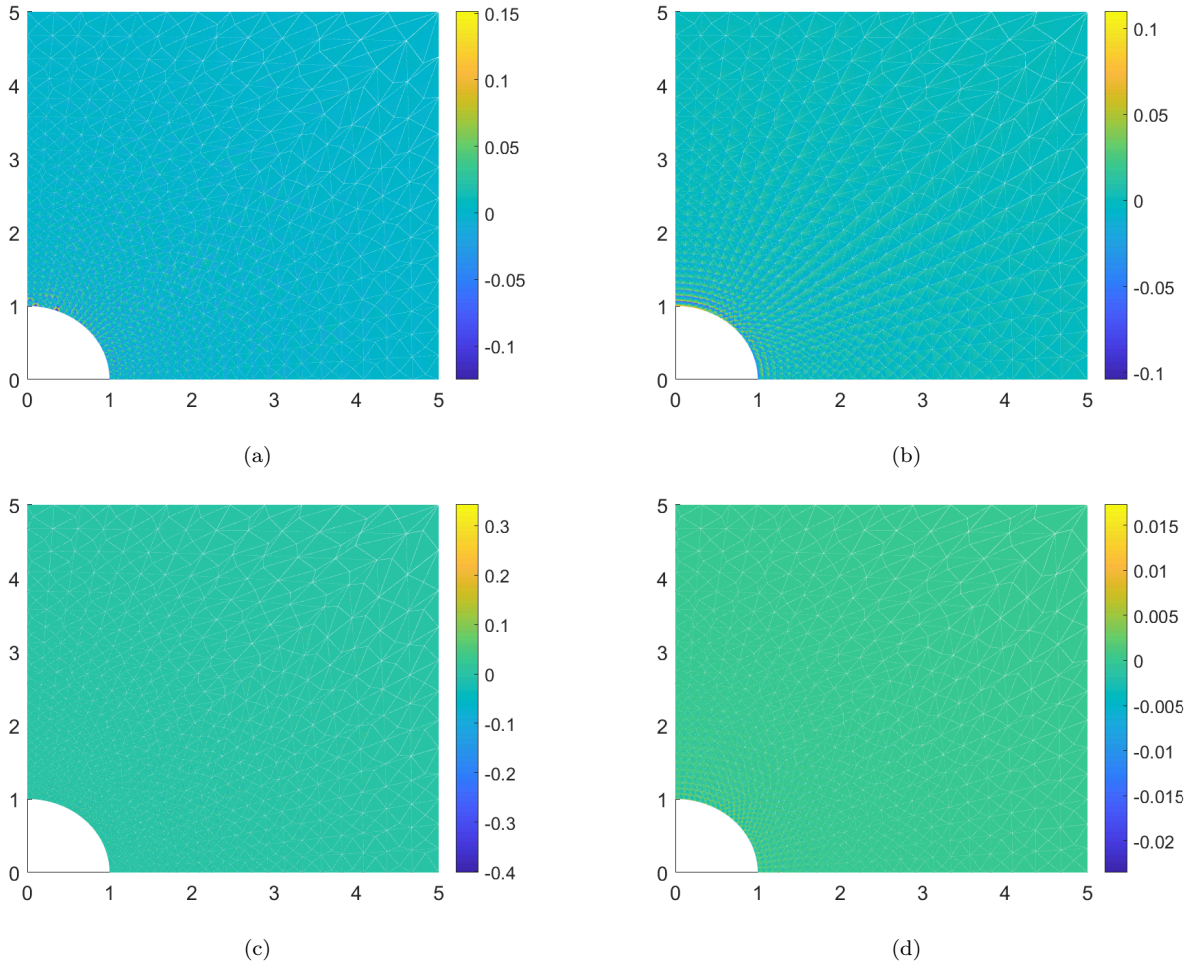


Figure 26: Contour plots of the error $\tilde{p} - \tilde{p}_h$ in hydrostatic stress on perturbed meshes for the plate with a circular hole problem. (a) CT FEM, (b) B-bar VEM, (c) SH-VEM, and (d) PSH-VEM.

penalty approach attains third and fourth order superconvergence in the energy seminorm and hydrostatic stress L^2 norm, respectively. The contour plots in Figure 32 show that for CT FEM, B-bar VEM, and SH-VEM, the errors are concentrated near the inner radius. The

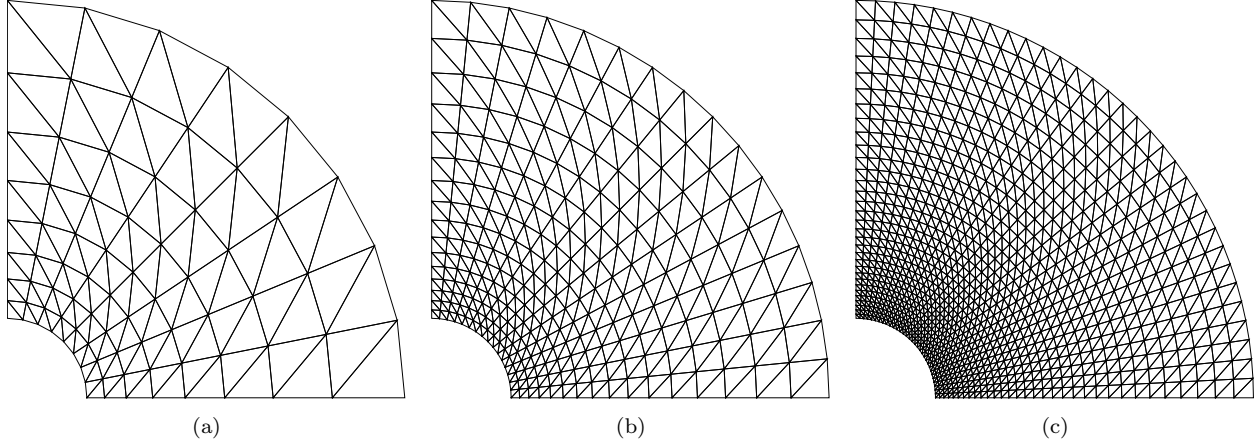


Figure 27: Structured triangular meshes for the hollow cylinder problem. (a) 128 elements, (b) 512 elements, and (c) 2048 elements.

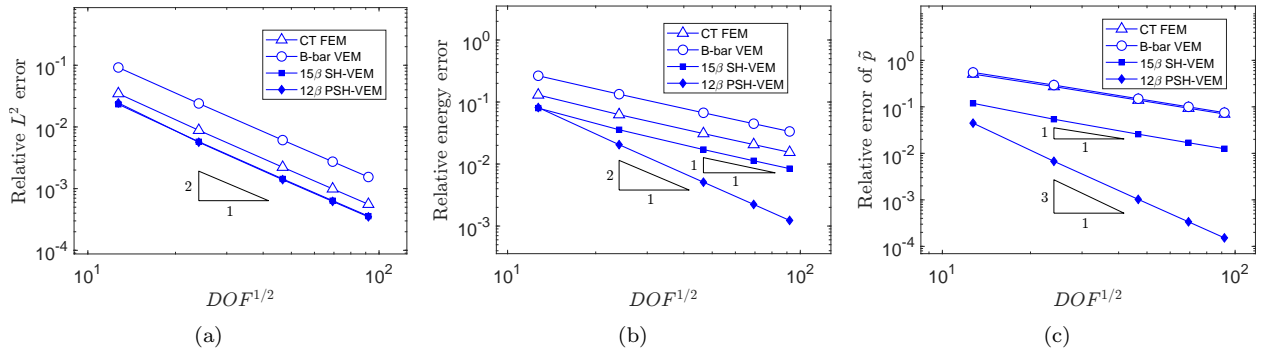


Figure 28: Comparison of CT FEM, B-bar VEM, SH-VEM, and PSH-VEM for the pressurized cylinder problem on structured meshes. (a) L^2 error of displacement, (b) energy error, and (c) L^2 error of hydrostatic stress.

largest error from SH-VEM is 9 percent, while both CT FEM and B-bar VEM produce much larger errors of 70 and 60 percent, respectively. For PSH-VEM, the errors are much smaller, with a maximum relative error of 0.4 percent.

Next, we examine the effects of the penalty parameter on the convergence rates of the pressurized cylinder problem. For simplicity, the material properties are set to be $E_Y = 1 \times 10^4$ psi and $\nu = 0.49995$. The problem is solved on structured triangular meshes (see Figure 27). The initial penalty parameter is $\alpha = \frac{10^4 \ell_0^2}{E_Y} = \ell_0^2$, so we test α in the range of $10^{-3} \ell_0^2$ to $10^3 \ell_0^2$. In Figure 33, we show the rates of convergence in the three error norms for different values of the penalty parameter α . The plots show that varying α did not affect the convergence of the displacement errors; however, the convergence of the energy seminorm is slightly affected and the rate of convergence in the L^2 norm of the hydrostatic stress is significantly reduced as α is decreased.

6.8. Manufactured problem

The basis functions derived from the Airy stress functions only satisfy the equilibrium conditions without a body force. Therefore, we test the convergence on a problem with

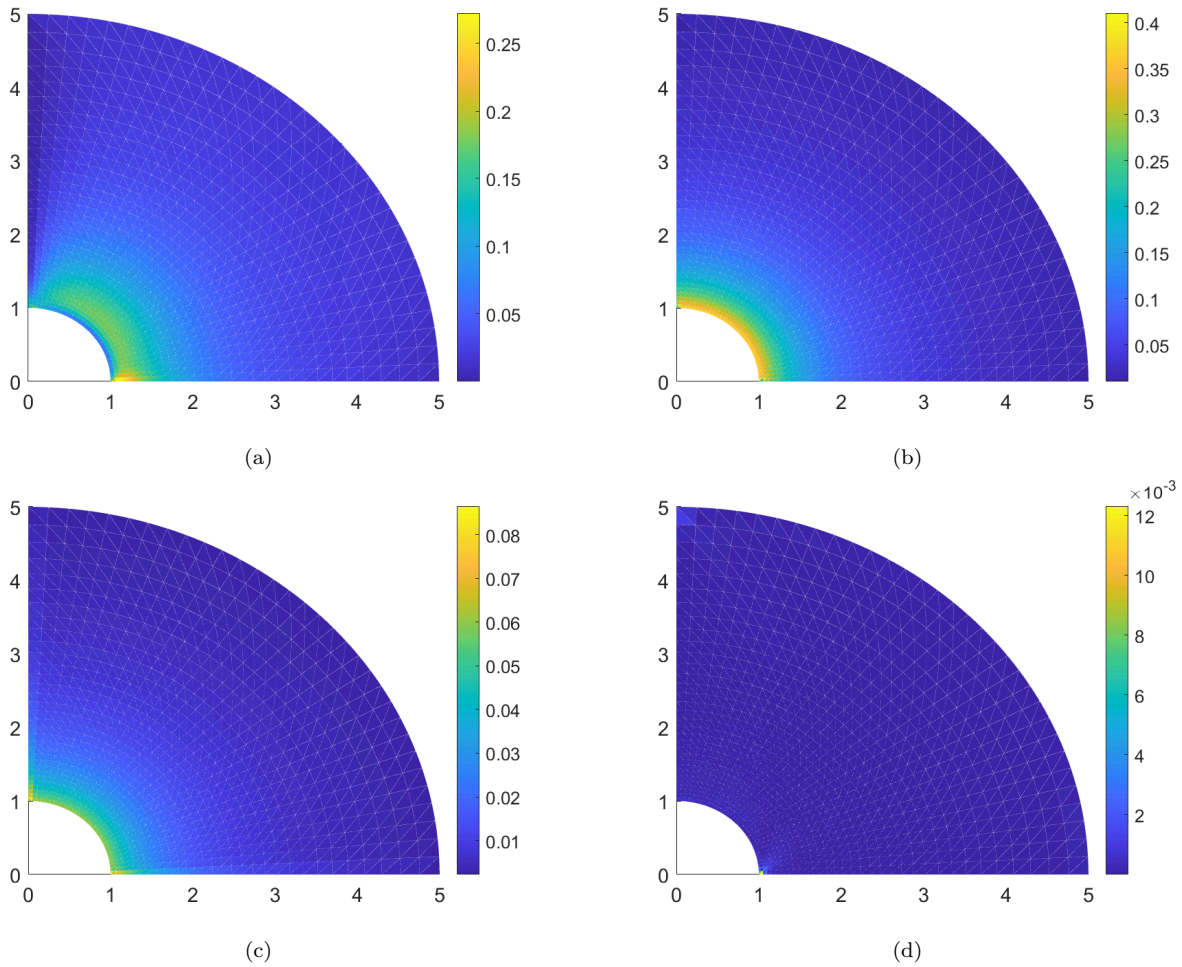


Figure 29: Contour plots of the relative error in the hydrostatic stress on structured meshes for the pressurized cylinder problem. The exact hydrostatic stress is 4166.528 psi. (a) CT FEM, (b) B-bar VEM, (c) SH-VEM, and (d) PSH-VEM.

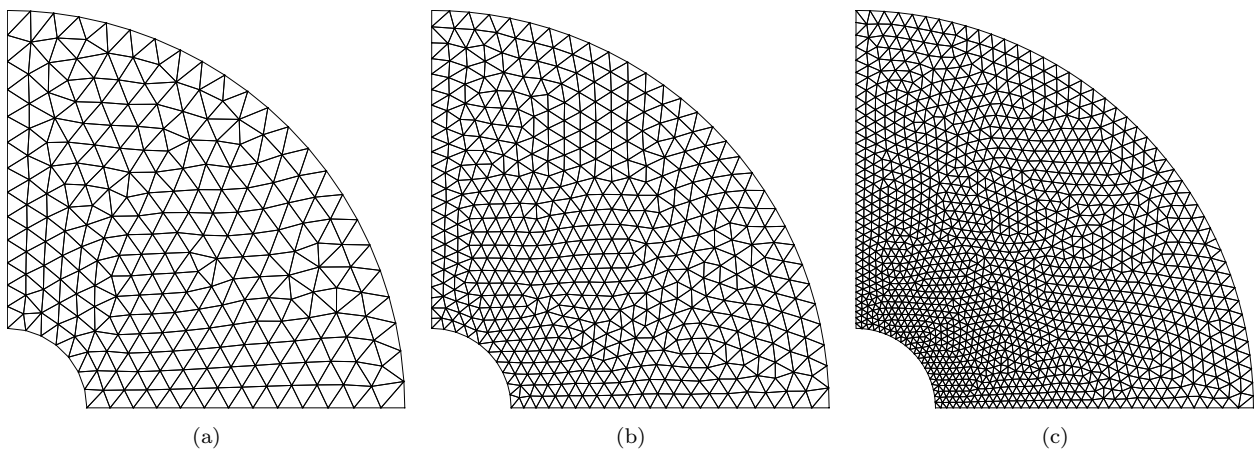


Figure 30: Unstructured triangular meshes for the hollow cylinder problem. (a) 500 elements, (b) 1000 elements, and (c) 2500 elements.

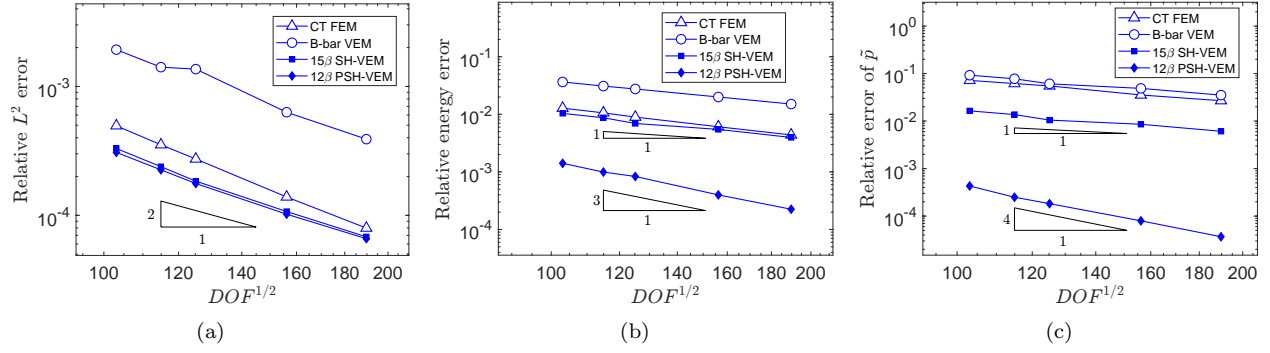


Figure 31: Comparison of CT FEM, B-bar VEM, SH-VEM, and PSH-VEM for the pressurized cylinder problem on unstructured meshes. (a) L^2 error of displacement, (b) energy error, and (c) L^2 error of hydrostatic stress.

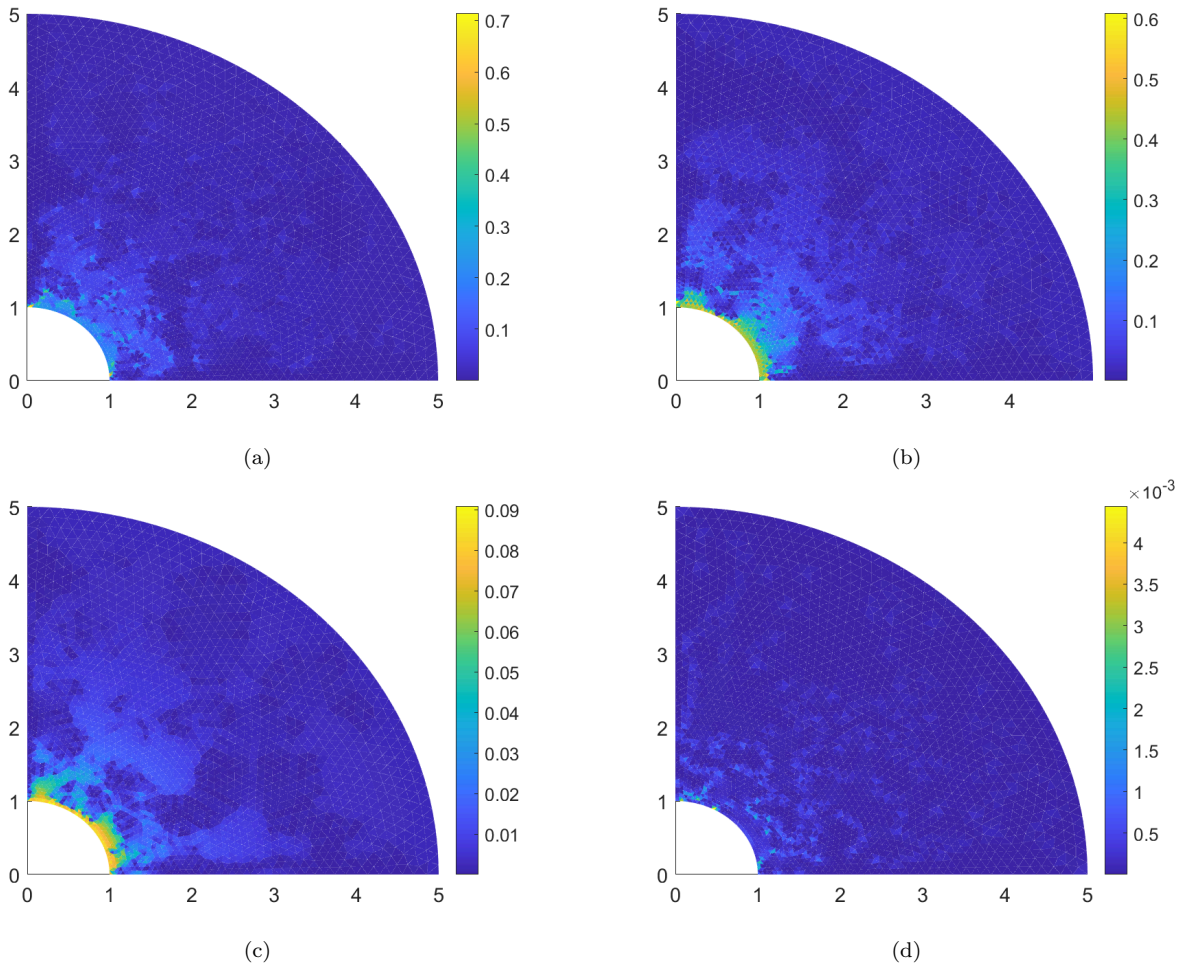


Figure 32: Contour plots of the relative error in the hydrostatic stress on unstructured meshes for the pressurized cylinder problem. The exact hydrostatic stress is 4166.528 psi. (a) CT FEM, (b) B-bar VEM, (c) SH-VEM, and (d) PSH-VEM.

a nonzero body force. We consider a manufactured problem given in [59] with the exact

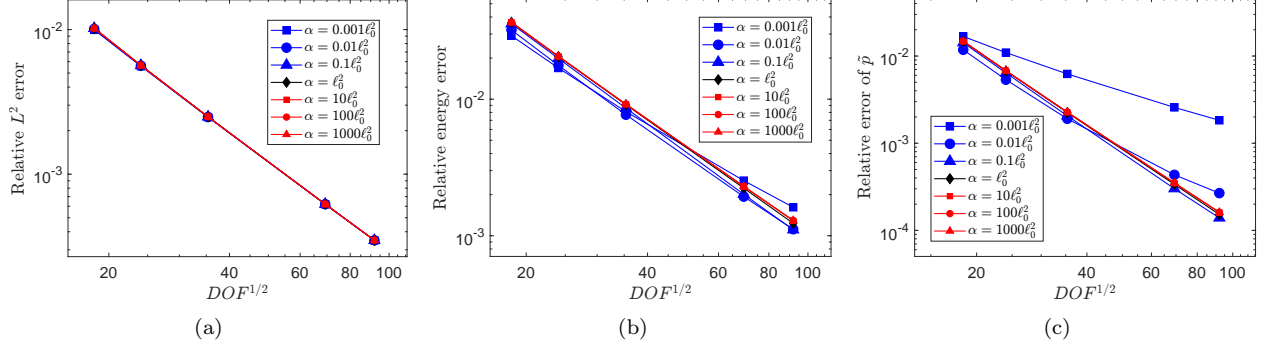


Figure 33: Comparison of the convergence of PSH-VEM for different choices of the penalty parameter α for the pressurized cylinder problem on structured meshes. (a) L^2 error of displacement, (b) energy error, and (c) L^2 error of hydrostatic stress.

solution and loading given by:

$$\begin{aligned}
 u(\mathbf{x}) &= \sin 2\pi y (\cos 2\pi x - 1) + \frac{1}{1 + \lambda} \sin \pi x \sin \pi y, \\
 v(\mathbf{x}) &= \sin 2\pi x (1 - \cos 2\pi y) + \frac{1}{1 + \lambda} \sin \pi x \sin \pi y, \\
 \mathbf{b}(\mathbf{x}) &= -\pi^2 \left\{ \begin{aligned} &\left(\frac{\lambda + \mu}{\lambda + 1} \right) \cos \pi(x + y) - \mu(8 \cos 2\pi x \sin 2\pi y - 4 \sin 2\pi y + \frac{2}{\lambda + 1} \sin \pi x \sin \pi y) \\ &\left(\frac{\lambda + \mu}{\lambda + 1} \right) \cos \pi(x + y) - \mu(-8 \cos 2\pi y \sin 2\pi x + 4 \sin 2\pi x + \frac{2}{\lambda + 1} \sin \pi x \sin \pi y) \end{aligned} \right\},
 \end{aligned}$$

where λ and μ are the first and second Lamé parameters given by

$$\lambda = \frac{E_Y \nu}{(1 + \nu)(1 - 2\nu)}, \quad \mu = \frac{E_Y}{2(1 + \nu)}.$$

For this problem, the material properties are set to $E_Y = 1$ psi and $\nu = 0.49995$. The first set of meshes we use is a perturbed unstructured triangular mesh. A few sample meshes are shown in Figure 34. The plots in Figure 35 show that the four methods converge optimally in displacement L^2 norm, energy seminorm, and hydrostatic stress L^2 norm. The PSH-VEM has smaller errors in both the energy and hydrostatic stress, but does not reach second order superconvergence. The contour plots in Figure 36 reveal that large errors in CT FEM appear along the boundary, while the other three methods have smooth hydrostatic stress fields.

Now, we solve the manufactured problem on a series of structured meshes. The meshes are generated by taking a uniform quadrilateral mesh, then splitting each element along the diagonal into two triangles. Then each triangular element is split into three pieces; a few representative meshes are shown in Figure 37. As was the case with the perturbed meshes, Figure 38 shows that all four methods deliver optimal convergence rates. The PSH-VEM again has the smallest errors in energy and hydrostatic stress, while the SH-VEM has the largest errors in hydrostatic stress. The contour plots in Figure 39 are relatively smooth and do not show large errors along the boundary.

Remark 4. From the sensitivity analysis of the beam and hollow cylinder, we know that if α is three orders of magnitude smaller than $\frac{10^4 \ell_0^2}{E}$, then the convergence rates in energy

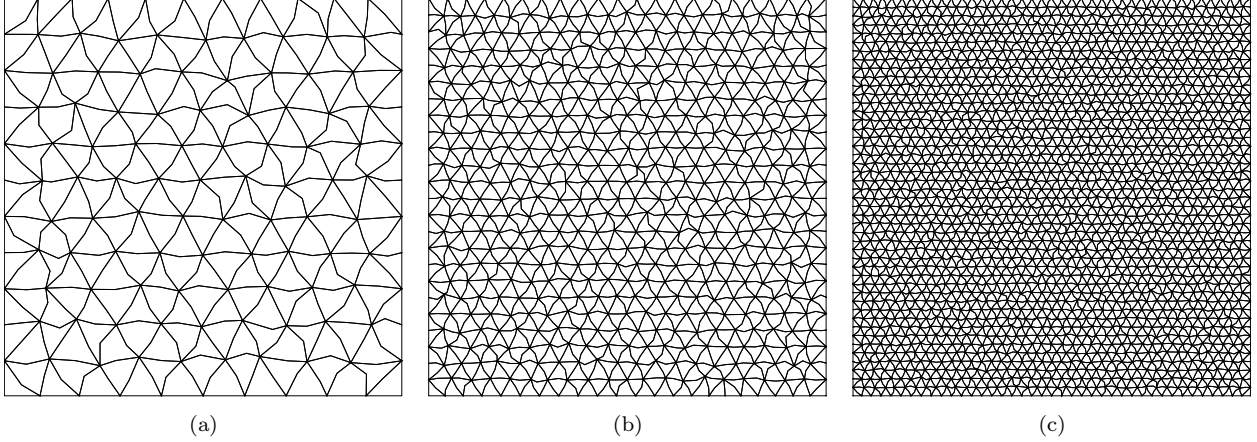


Figure 34: Perturbed triangular meshes for the manufactured problem. (a) 200 elements, (b) 1000 elements, and (c) 3600 elements.

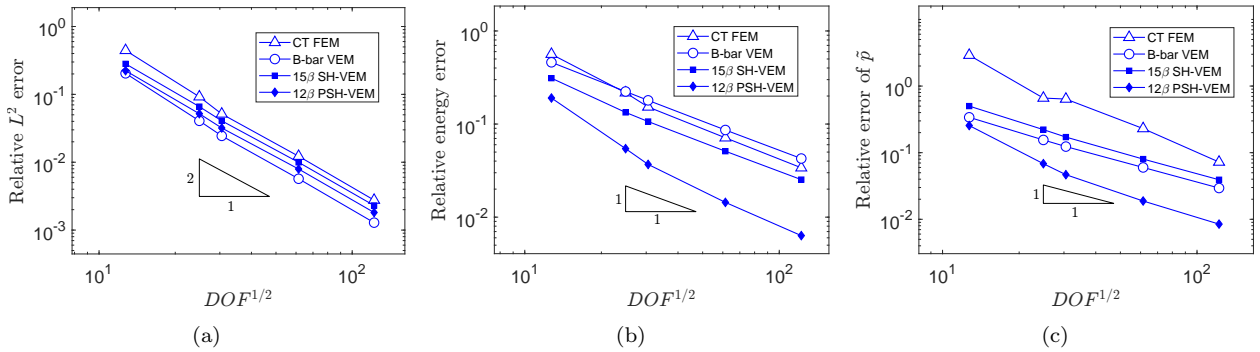


Figure 35: Comparison of CT FEM, B-bar VEM, SH-VEM, and PSH-VEM for the manufactured problem on perturbed meshes. (a) L^2 error of displacement, (b) energy error, and (c) L^2 error of hydrostatic stress.

seminorm and L^2 norm of the hydrostatic stress are affected. For this manufactured problem, when using a Young's modulus $E_Y = 1$ psi and α given in (34), the penalty parameter is set to the minimum value $\alpha = 10\ell_0^2$. This value is three orders of magnitude less than $\frac{10^4 \ell_0^2}{E}$; therefore, the errors of energy and hydrostatic stress are not expected to have higher order convergence rates even for uniform meshes. However, from our numerical tests, having a larger E_Y or increasing the upper bound on the penalty parameter α results in superconvergent solutions on sufficiently regular meshes.

6.9. Punch problem

Next, we adapt the problem of a punch being driven into a solid as described in [71] for nearly incompressible hyperelastic materials. This problem is used in [71] to test the robustness of mixed virtual element methods for large deformations and to compare to standard mixed finite element formulations. In our tests, we assume a linearly elastic material and solve the problem on a unit square domain using $E_Y = 250$ psi and $\nu = 0.4999999$. The left and top edges are horizontally constrained, while the bottom edge is vertically constrained. Along half of the top edge, a uniform load of $F = -250$ lbf per unit length is applied. For this problem, we examine the three methods B-bar VEM, SH-VEM, and PSH-

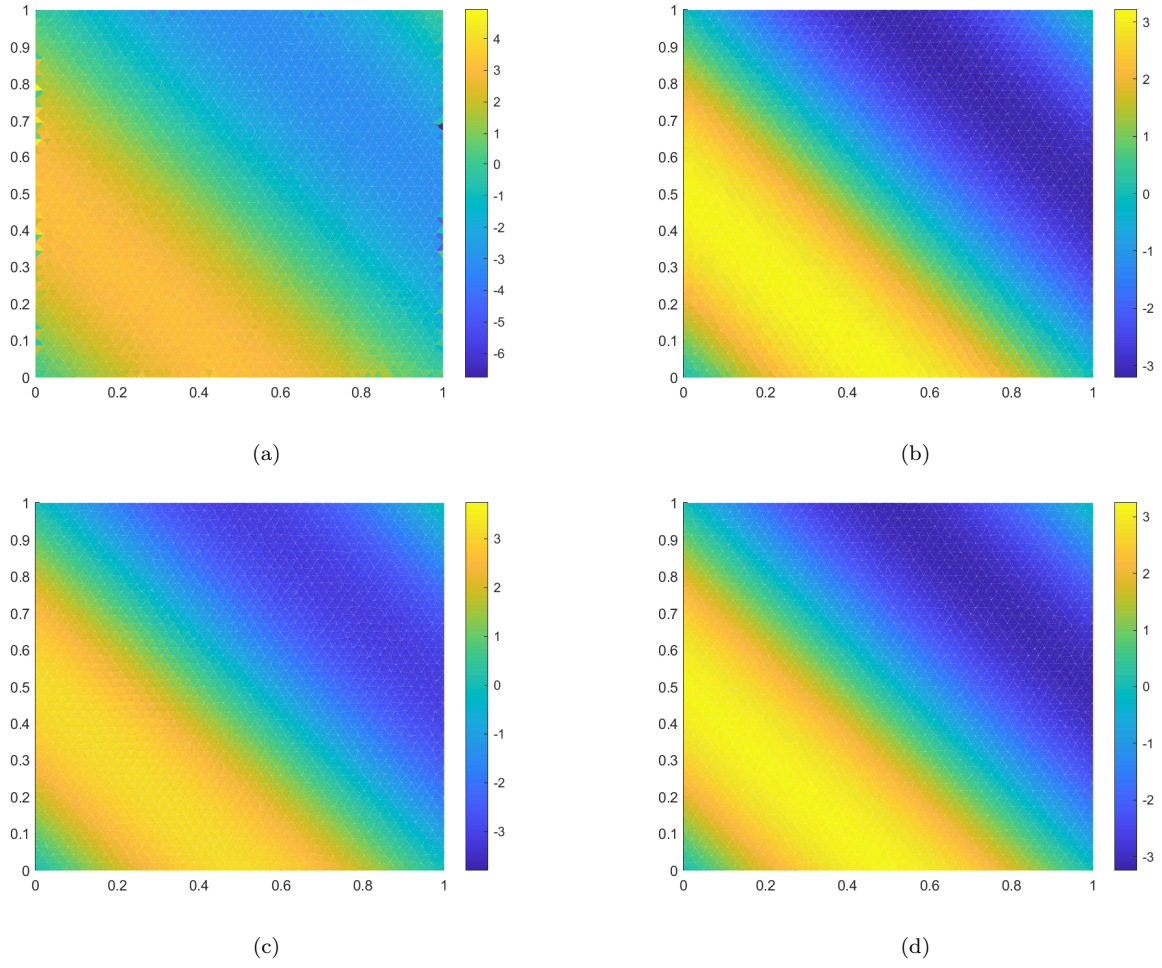


Figure 36: Contour plots of the hydrostatic stress on perturbed meshes for the manufactured problem. (a) CT FEM, (b) B-bar VEM, (c) SH-VEM, and (d) PSH-VEM.

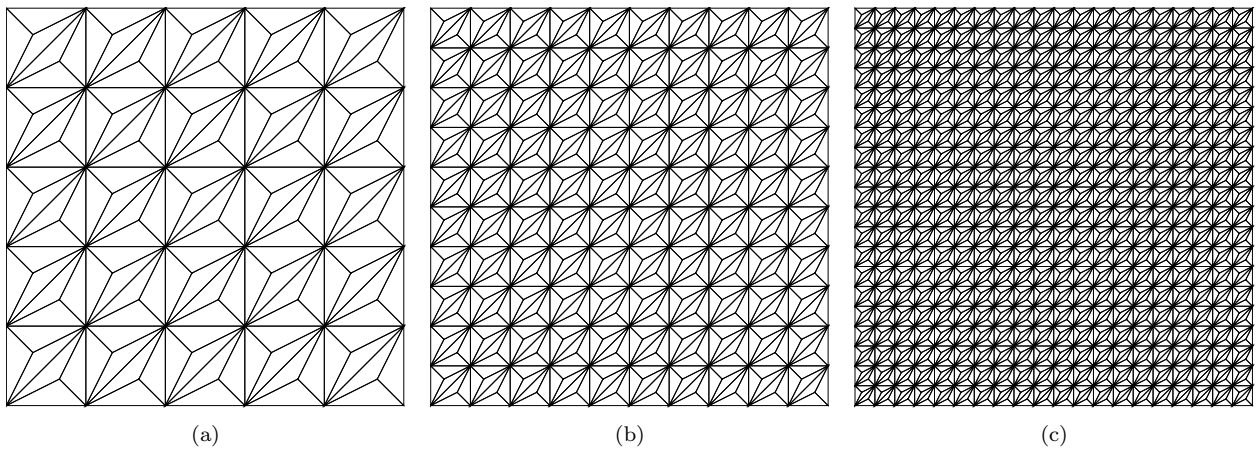


Figure 37: Structured triangular meshes for the manufactured problem. (a) 150 elements, (b) 600 elements, and (c) 2400 elements.

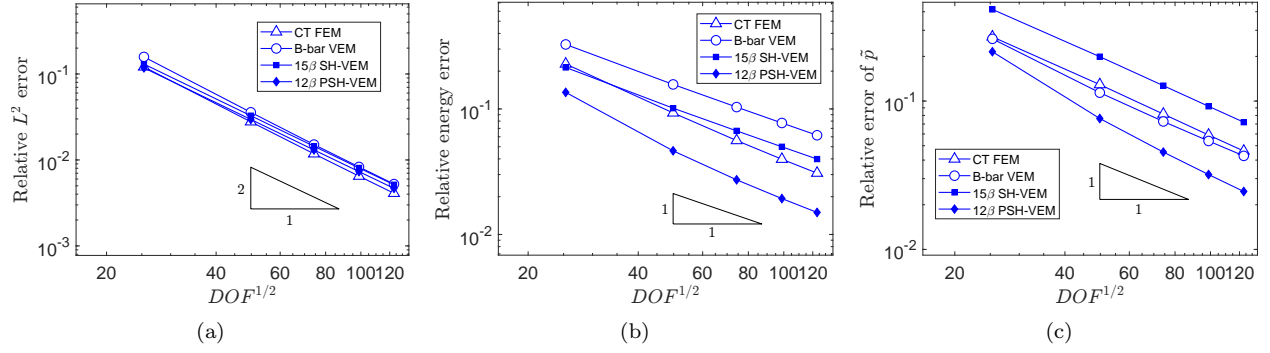


Figure 38: Comparison of CT FEM, B-bar VEM, SH-VEM, and PSH-VEM for the manufactured problem on structured meshes. (a) L^2 error of displacement, (b) energy error, and (c) L^2 error of hydrostatic stress.

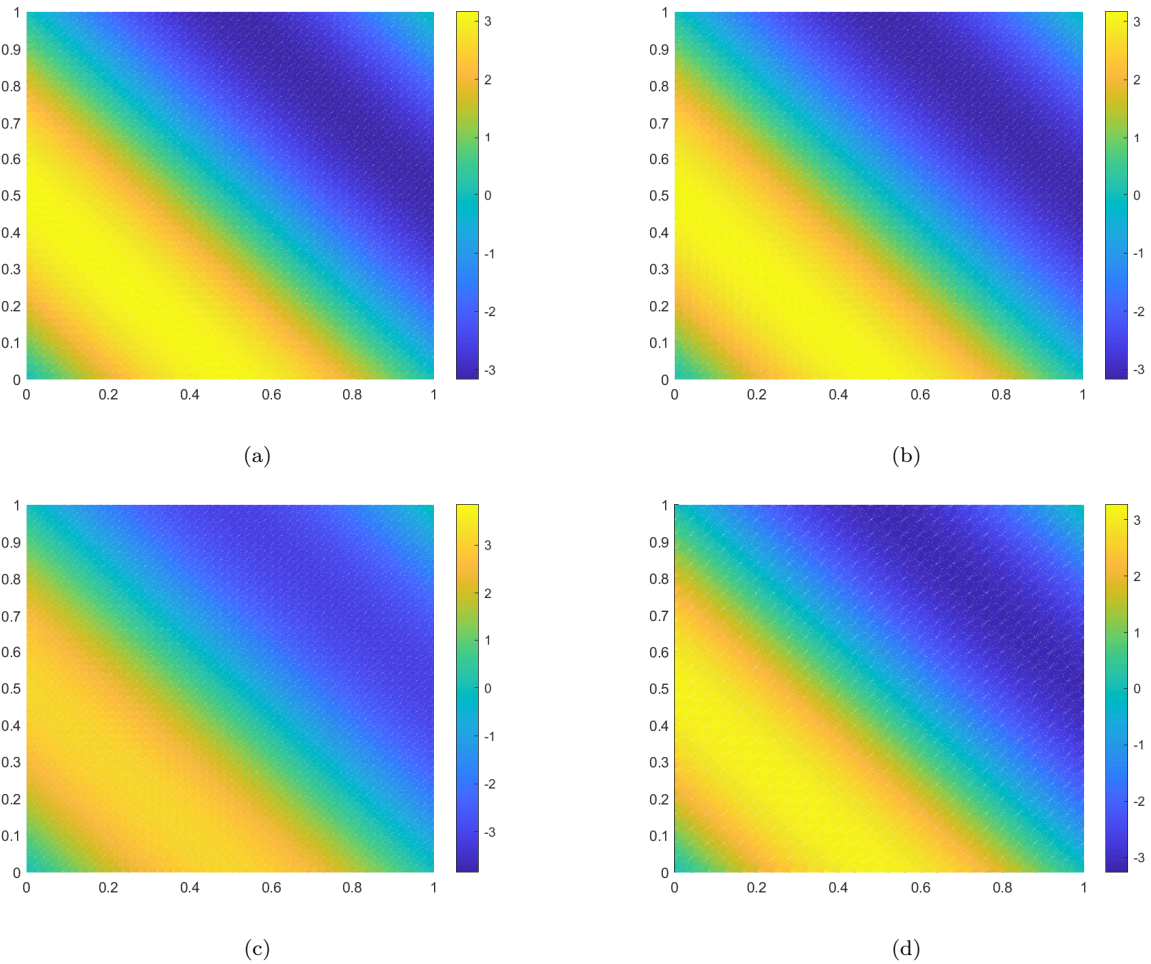


Figure 39: Contour plots of the hydrostatic stress on structured meshes for the manufactured problem. (a) CT FEM, (b) B-bar VEM, (c) SH-VEM, and (d) PSH-VEM.

VEM. We first use an unstructured triangular mesh (see Figure 40a) and plot the resulting contours of the hydrostatic stress in Figure 40. The contours are plotted on the deformed configuration. From the plots, we find that the three methods produced relatively smooth

hydrostatic stress fields, with B-bar and PSH-VEM having a similar range. In Figure 41, plots of the trace of the strain field are shown on the undeformed configuration. The three methods yielded nearly traceless strain fields, which is consistent for a nearly incompressible material.

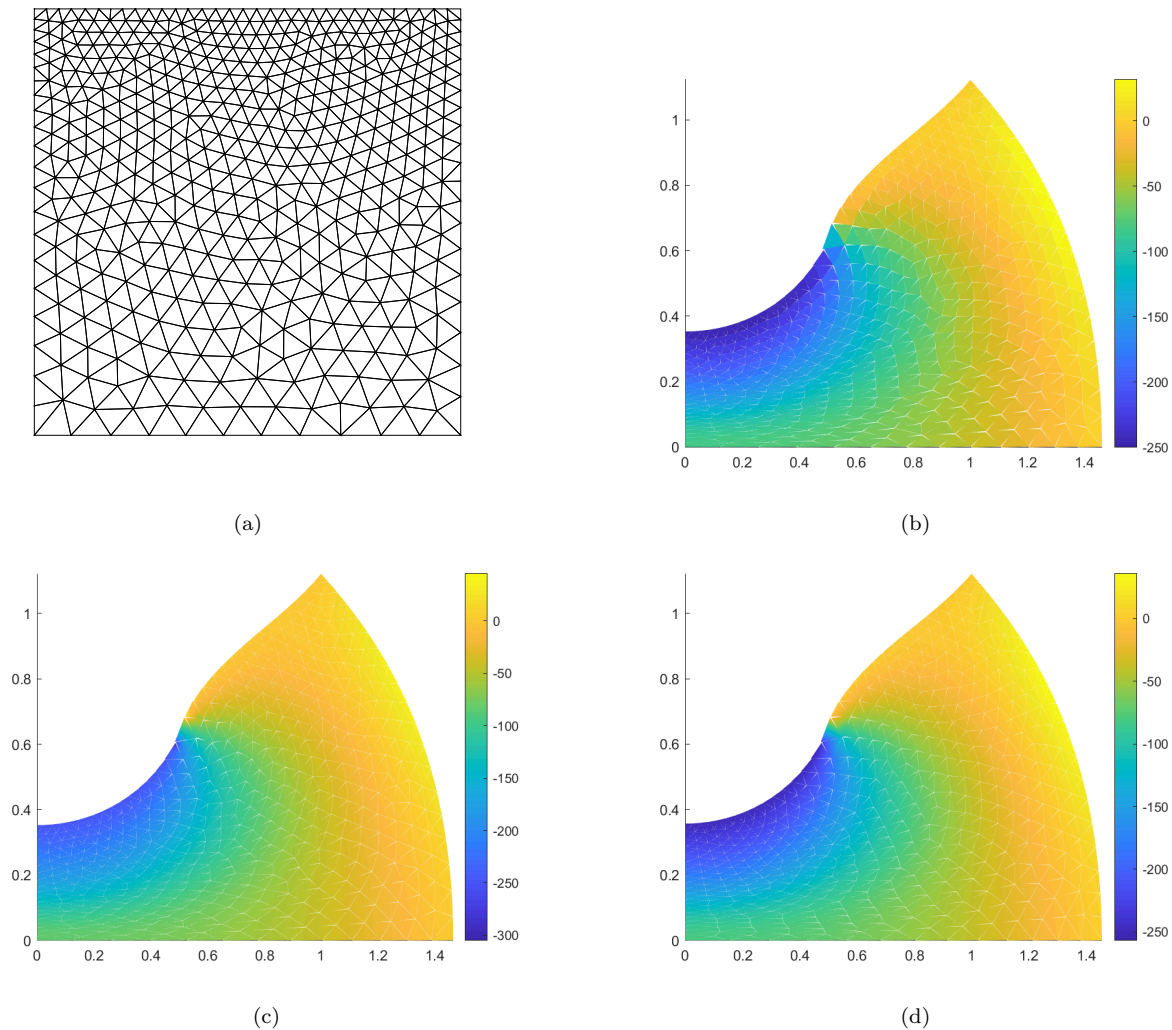


Figure 40: (a) Representative unstructured mesh for the punch problem. Contour plots of the hydrostatic stress for the punch problem plotted on the deformed configuration using unstructured meshes. (b) B-bar VEM, (c) SH-VEM, and (d) PSH-VEM.

Next, we use a mesh with convex and nonconvex elements with an example mesh shown in Figure 42a. The contour plots of the hydrostatic stress are given in Figure 42. The plots show that even for nonconvex elements, the three methods retain relatively smooth hydrostatic stress fields. In Figure 43, the contours of the trace of the strain field is presented. Similar to the unstructured case, the strain field of the three methods are nearly traceless.

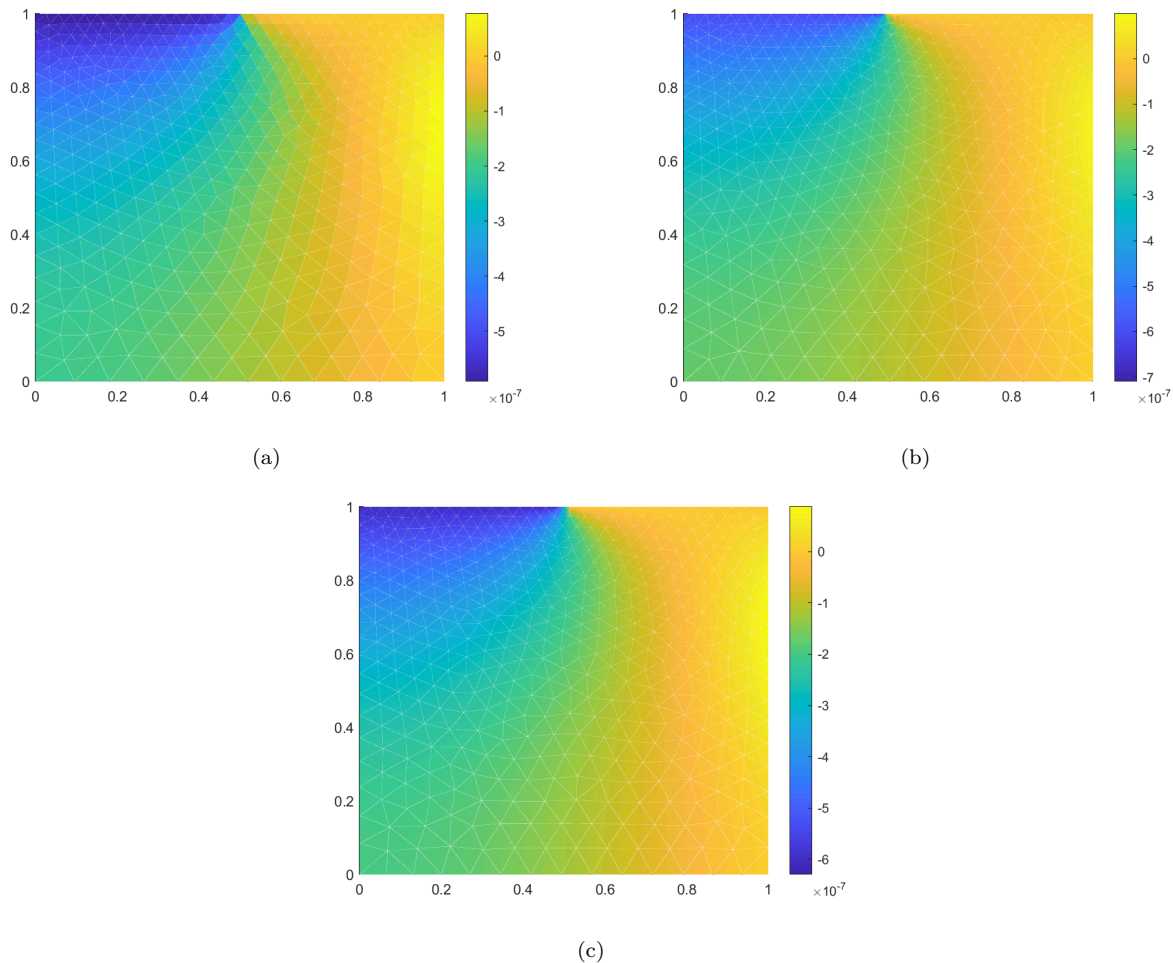


Figure 41: Contour plots of the trace of the strain field for the punch problem plotted on the undeformed configuration using structured meshes. (a) B-bar VEM, (b) SH-VEM, and (c) PSH-VEM.

7. Conclusion

In this paper, we studied an extension of the stress-hybrid virtual element method [20] to first-order six-noded triangular virtual elements for linear elastic problems. Since complex geometries are amenable to Delaunay mesh generation, this work is a first attempt to study two-dimensional virtual element formulations for incompressible elasticity on general triangular meshes (including Delaunay meshes). In this approach, we used the Hellinger–Reissner variational principle to construct a weak equilibrium and strain-displacement conditions. The weak strain-displacement condition is used along with the virtual element formulation to define a computable projection operator for the stress field. In the initial approach, we used a divergence-free polynomial tensor basis and by combining it with the divergence theorem, we were able to compute the stress projection with only the displacements along the boundary. When using a nondivergence-free basis, we relied on the modification of the VEM space introduced in [11] and a secondary energy projection to recover the stress projection. However, we found that this requirement is rather restrictive and leads to elements being overly stiff. Therefore, we relaxed the condition by introducing a penalty term to weakly sat-

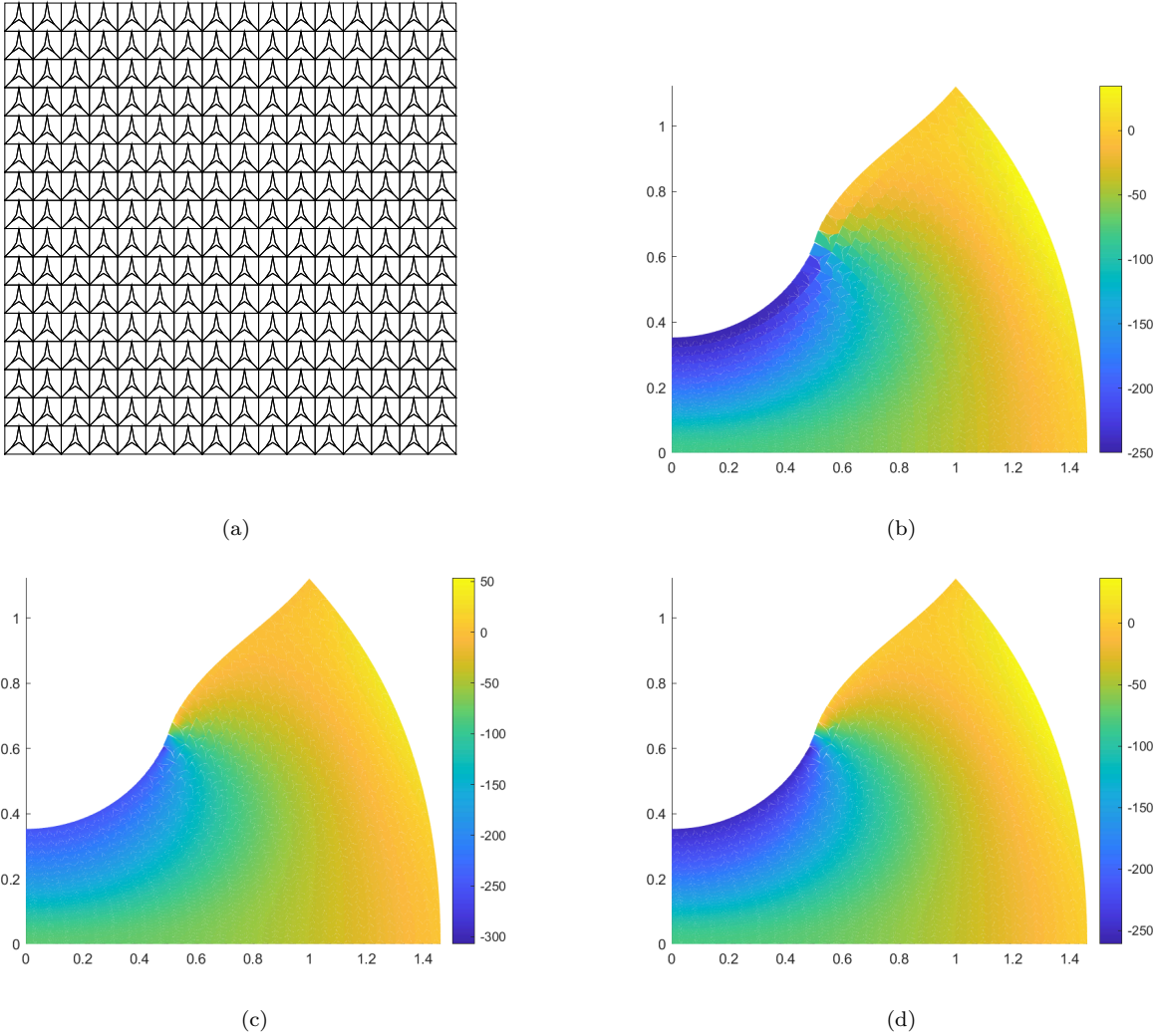


Figure 42: (a) Representative nonconvex mesh for the punch problem. Contour plots of the hydrostatic stress of PSH-VEM for the punch problem plotted on the deformed configuration using nonconvex meshes. (b) B-bar VEM, (c) SH-VEM, and (d) PSH-VEM.

isfy the element equilibrium condition and alleviate locking. The SH and PSH-formulations were then tested for stability using an eigenvalue analysis. For the divergence-free basis, a 15-term expansion was used to ensure no zero-energy modes appeared for highly distorted elements, while a complete bilinear 12-term expansion was used for the penalty element. For the thin cantilever beam and Cook’s membrane problems we found both SH-VEM and PSH-VEM were not sensitive to shear locking. The PSH-VEM was able to reproduce nearly exact bending solutions even on coarse meshes. For the plate with a circular hole and pressurized cylinder the stress-hybrid method produced optimal convergence rates in the L^2 norm of the displacement, energy seminorm, and L^2 norm of the hydrostatic stress; while the penalty formulation produced superconvergent rates in energy seminorm and L^2 norm of the hydrostatic stress. The plate with a hole had relatively smooth hydrostatic stress fields, while for the pressurized cylinder it was observed that large errors concentrated around the interior

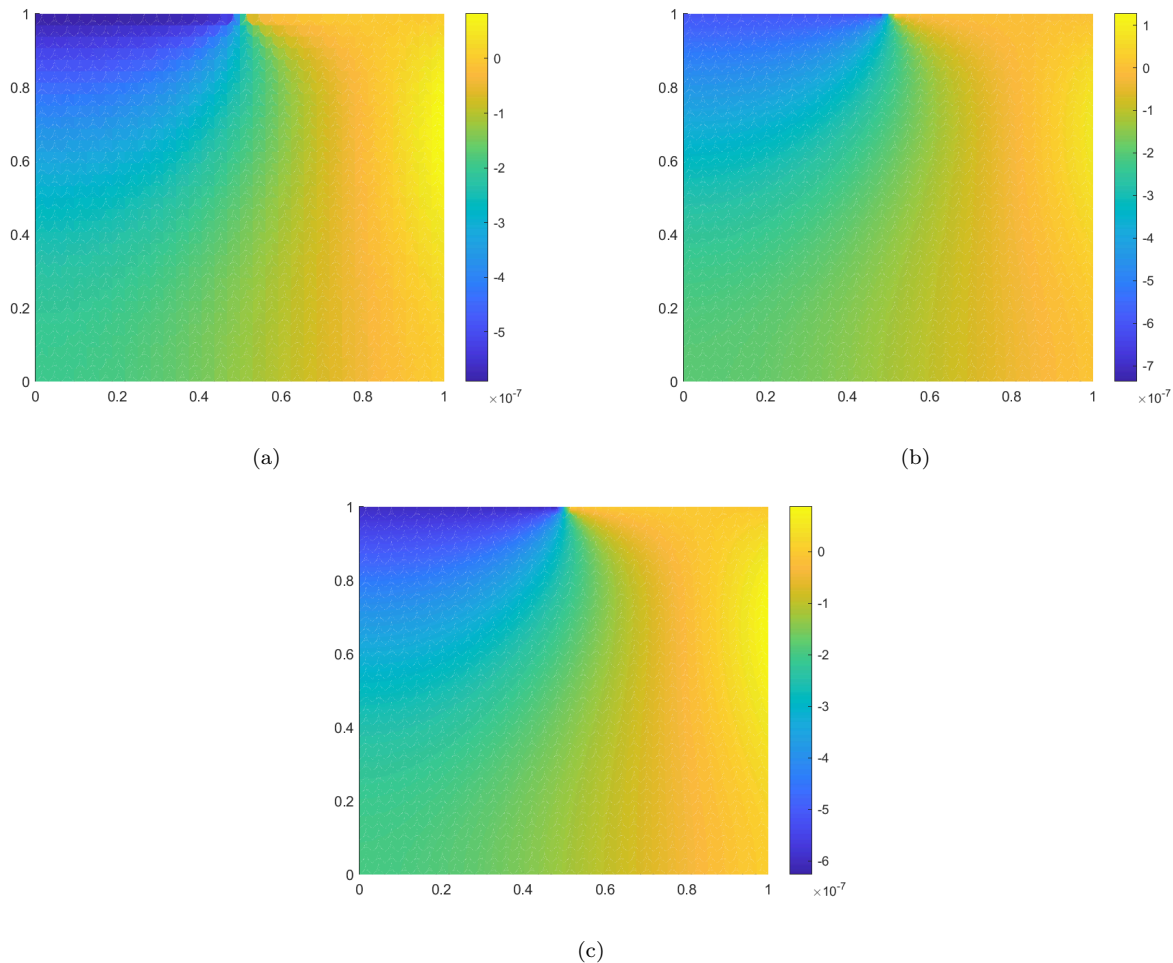


Figure 43: Contour plots of the trace of the strain field for the punch problem plotted on the undeformed configuration using nonconvex meshes. (a) B-bar VEM, (b) SH-VEM, and (c) PSH-VEM.

boundary but the stress-hybrid methods were more accurate. In the manufactured problem, SH-VEM and PSH-VEM showed no signs of locking and had relatively smooth contours of hydrostatic stress. The PSH-VEM showed better accuracy for the manufactured problem; however, for our choice of penalty parameter, the PSH-VEM did not achieve superconvergent rates for the energy seminorm or L^2 norm of the hydrostatic stress. For the punch problem, both SH-VEM and PSH-VEM did not show instabilities in the hydrostatic stress field and produced nearly traceless strain fields. In the Appendix, we examined a stabilized version of the 9β SH-VEM and 11β SH-VEM. The 9β and 11β SH-VEM uses a 9-term and 11-term divergence-free basis, respectively. The stress-hybrid methods were then tested on additional benchmark problems. An eigenvalue analysis was used to test stability and volumetric locking of the two stress-hybrid methods. The thick cantilever beam problem showed that the stabilized methods with fewer basis functions were less stiff in bending. The plate with a hole problem showed that the stress-hybrid approaches converged optimally in all cases. The two stabilized methods attained better accuracy than 15β SH-VEM, with 9β SH-VEM having performance that is more comparable to the penalized approach. From these tests, we found

that the two stabilized stress-hybrid formulations did not show signs of volumetric locking and did not have spurious eigenvalues. As part of future work, finding optimal stress basis functions, incorporating additional techniques to mitigate volumetric locking and extending the stress-hybrid and penalty stress-hybrid virtual element method to nonlinear and three dimensional problems are of interest.

Acknowledgements

The research support of Sandia National Laboratories to the University of California, Davis, is gratefully acknowledged. Sandia National Laboratories is a multi-mission laboratory managed and operated by National Technology & Engineering Solutions of Sandia, LLC (NTESS), a wholly owned subsidiary of Honeywell International Inc., for the U.S. Department of Energy’s National Nuclear Security Administration (DOE/NNSA) under contract DE-NA0003525. This written work is authored by an employee of NTESS. The employee, not NTESS, owns the right, title, and interest in and to the written work and is responsible for its contents. Any subjective views or opinions that might be expressed in the written work do not necessarily represent the views of the U.S. Government. The publisher acknowledges that the U.S. Government retains a non-exclusive, paid-up, irrevocable, world-wide license to publish or reproduce the published form of this written work or allow others to do so, for U.S. Government purposes. The DOE will provide public access to results of federally sponsored research in accordance with the DOE Public Access Plan.

Appendix A. Stabilized stress-hybrid methods

In the standard virtual element method, a stabilization term is necessary to ensure that the element stiffness matrix has correct rank. For completeness, we examine effects of a stabilization term on the two methods 9β SH-VEM and 11β SH-VEM, which were shown earlier to have zero-energy modes. The 9β SH-VEM is constructed from the first 9 terms of the basis given in (14), while the 11β SH-VEM uses the first 11 terms. For the stability term, we follow the construction given in [2]:

$$\mathbf{K}_S = \tau [\mathbf{I} - \mathbf{D}(\mathbf{D}^T \mathbf{D})^{-1} \mathbf{D}^T], \quad (\text{A.1a})$$

where τ is a scaling factor, \mathbf{I} is the identity matrix and $\mathbf{D} \in \mathbb{R}^{12 \times 6}$ is the matrix containing the degrees of freedom of the polynomials $\mathbf{m}_\alpha \in \widehat{\mathcal{M}}(E)$ given by

$$\mathbf{D} = \begin{bmatrix} \mathbf{m}_1(\mathbf{x}_1) & \mathbf{m}_2(\mathbf{x}_1) & \dots & \mathbf{m}_6(\mathbf{x}_1) \\ \mathbf{m}_1(\mathbf{x}_2) & \mathbf{m}_2(\mathbf{x}_2) & \dots & \mathbf{m}_6(\mathbf{x}_2) \\ \dots & \dots & \dots & \dots \\ \mathbf{m}_1(\mathbf{x}_6) & \mathbf{m}_2(\mathbf{x}_6) & \dots & \mathbf{m}_6(\mathbf{x}_6) \end{bmatrix}. \quad (\text{A.1b})$$

It is common to choose the scaling factor to be proportional to the trace of the element stiffness matrix \mathbf{K}_E ; however, this choice of scaling will lead to an overly stiff solution for nearly incompressible materials [49, 56]. For simplicity, we set $\tau = \frac{1}{2}$ in the following examples. The stabilized element stiffness matrix is then given by

$$\mathbf{K} = \mathbf{K}_E + \mathbf{K}_S. \quad (\text{A.2})$$

Appendix A.1. Eigenvalue analysis

We first repeat the eigenvalue analysis presented in Section 6.1. Contour plots for the fourth smallest eigenvalue are presented in Figure A.1. The plots reveal that the stabilization term has eliminated the spurious eigenvalue for both 9β SH-VEM and 11β SH-VEM.

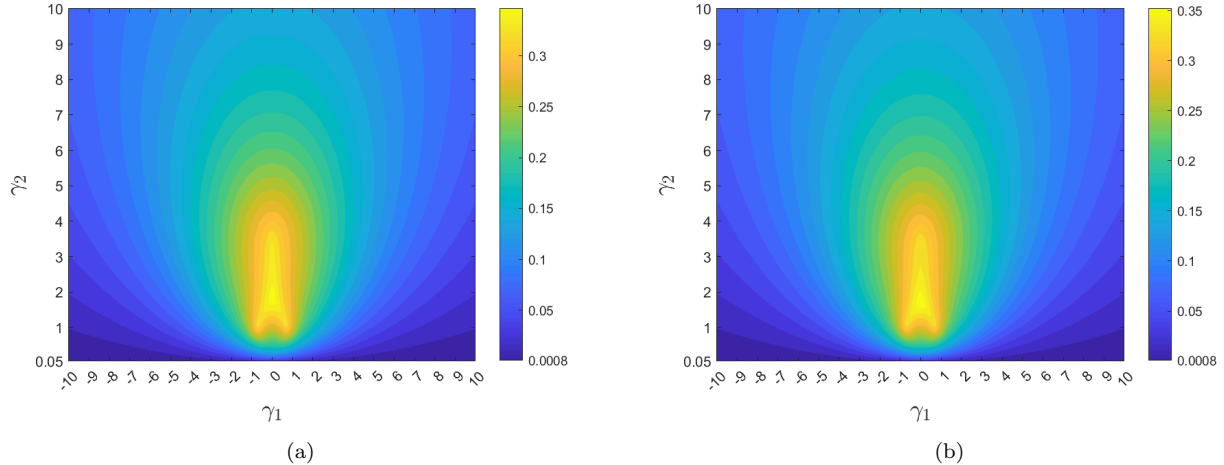


Figure A.1: Contour plots of the fourth smallest eigenvalue of (a) stabilized 9β SH-VEM and (b) stabilized 11β SH-VEM.

Next, we repeat the eigenvalue analysis in Section 6.3 to test for locking in the near-incompressible limit. The five largest eigenvalues of the element stiffness matrix for 9β and 11β SH-VEM are given in Table A.1 for a regular six-noded triangular element and in Table A.2 for a nonconvex element. The tables show that both methods only have a single eigenvalue that tends toward infinity. This suggests that the two stabilized elements are not prone to volumetric locking.

9β SH-VEM	11β SH-VEM
7.8×10^{-1}	9.0×10^{-1}
1.2×10^0	1.3×10^0
1.3×10^0	1.5×10^0
4.6×10^0	4.6×10^0
4.2×10^6	4.2×10^6

Table A.1: Comparison of the five largest eigenvalues of the element stiffness matrix on a six-noded triangular element.

Appendix A.2. Bending of a thick cantilever

We consider the bending of a cantilever beam under plane stress conditions with a shear end load as shown in [30, 31] for different triangular elements. The material has a Young’s modulus $E_Y = 30000$ psi and Poisson’s ratio $\nu = 0.25$. The beam has a length of $L = 48$ inch, a height of $D = 12$ inch, and unit thickness. A shear load of $P = 40$ lbf is applied on the right boundary, while the left boundary is fixed. For this problem, we compare the

9β SH-VEM	11β SH-VEM
5.9×10^{-1}	7.9×10^{-1}
1.8×10^0	1.8×10^0
2.1×10^0	4.9×10^0
9.9×10^0	9.9×10^0
6.7×10^6	6.7×10^6

Table A.2: Comparison of the five largest eigenvalues of the element stiffness matrix on a six-noded nonconvex element.

tip displacement of the stress-hybrid methods: 15β SH-VEM, 12β PSH-VEM, 9β SH-VEM, 11β SH-VEM, and the 5β SH-VEM for quadrilaterals given in [20]. The mesh for the 5β SH-VEM consists of $N \times N$ ($N = 1, 2, 4, 8, 16$) structured quadrilateral elements with an aspect ratio of 4 : 1, while the corresponding triangular mesh is constructed by splitting each quadrilateral element along a diagonal (see Figure A.2). In Table A.3, the normalized tip displacement for the different methods on each mesh is shown. The table shows that all the SH-VEM and PSH-VEM methods converge with mesh refinement, but the 15β SH-VEM, which uses higher order terms, is slightly stiffer. The other three methods on six-noded triangles have comparable performance to the 5β SH-VEM on quadrilaterals.

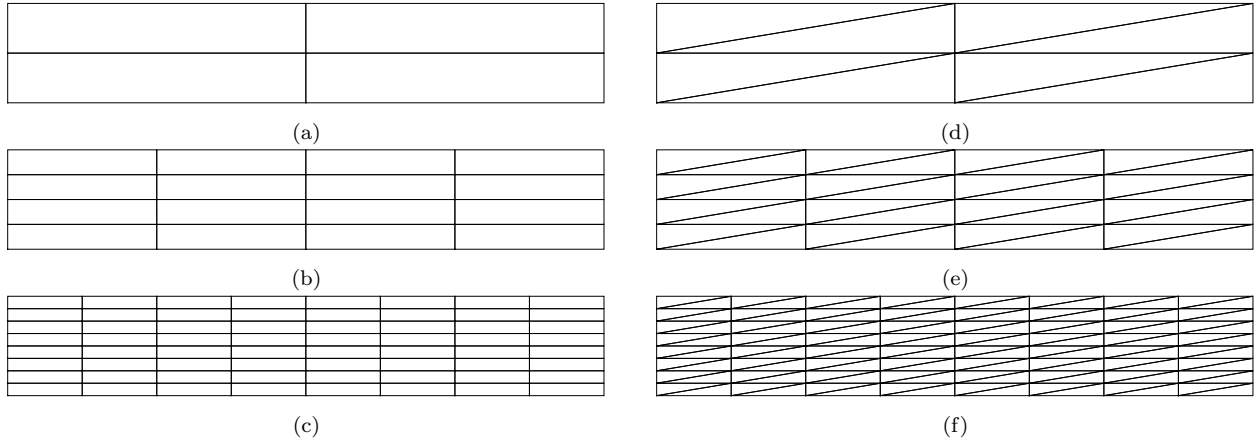


Figure A.2: Structured meshes for the thick cantilever beam problem. Meshes in (a)-(c) consists of quadrilaterals with an aspect ratio of 4 : 1 and (d)-(f) consist of triangular meshes where each corresponding quadrilateral element is cut along the diagonal.

Appendix A.3. Plate with a circular hole

Finally, we revisit the plate with a circular hole problem that is presented in Section 6. For this problem, we compare the convergence of the stress-hybrid methods: 15β SH-VEM, 12β PSH-VEM, 9β SH-VEM, 11β SH-VEM, and the 5β SH-VEM, in the error norms given in (36). We first test this problem on structured quadrilateral and triangular meshes with the same number of global degrees of freedom; a few sample meshes are shown in Figure A.3. In Figure A.4, the convergence results are given for the stress-hybrid methods and show that all the methods converge optimally in the displacement L^2 norm, energy seminorm and L^2

	5β SH-VEM	15β SH-VEM	12β PSH-VEM	9β SH-VEM	11β SH-VEM
1×1	0.7637	0.4536	1.6185	0.4798	0.4778
2×2	0.9413	0.8236	1.0665	0.8668	0.8612
4×4	0.9856	0.9610	1.0133	0.9787	0.9770
8×8	0.9965	0.9917	1.0030	0.9971	0.9966
16×16	0.9992	0.9982	1.0007	0.9997	0.9996

Table A.3: Comparison of the normalized tip displacements for the cantilever beam problem on structured meshes. The meshes are constructed from $N \times N$ ($N = 1, 2, 4, 8, 16$) quadrilaterals with aspect ratio of 4 : 1.

norm of the hydrostatic stress (the penalty approach attains superconvergence in energy and hydrostatic stress). The 5β SH-VEM has the smallest error in displacement, but the triangular SH-VEM have better accuracy in energy and hydrostatic stress, with the 12β PSH-VEM and 9β SH-VEM having the smallest errors.

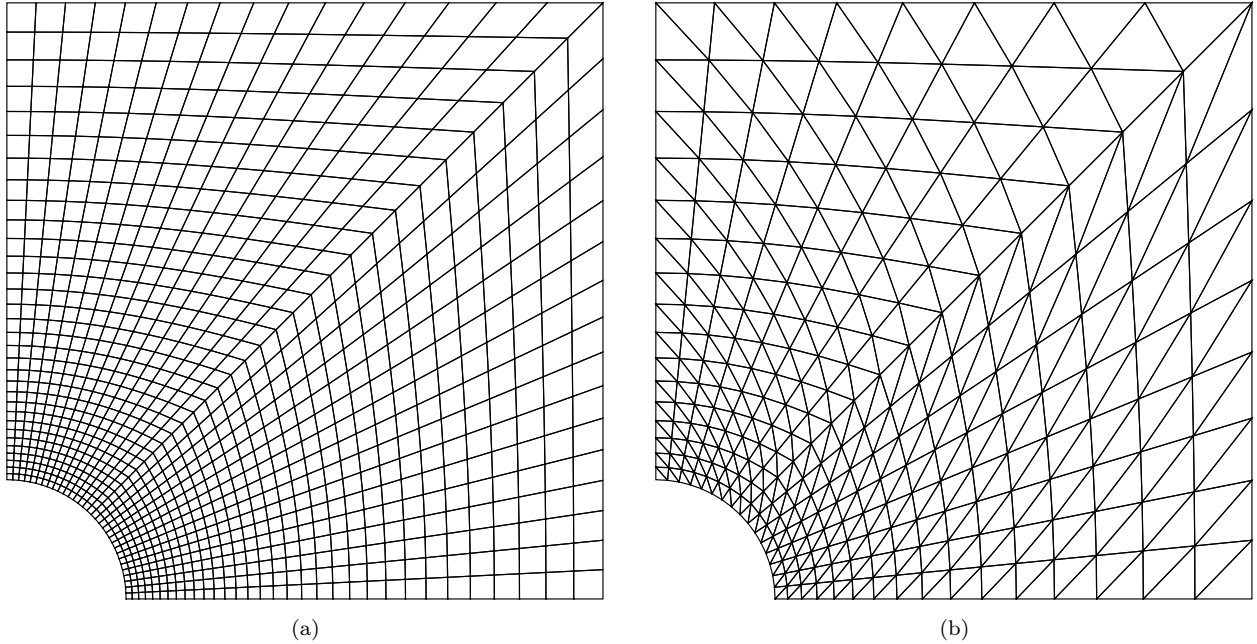


Figure A.3: (a) A structured quadrilateral mesh and (b) a structured triangular mesh with the same number of degrees of freedom for the plate with a hole problem.

We now test the plate with a circular hole problem on unstructured meshes. The quadrilateral meshes for 5β SH-VEM are constructed by taking unstructured triangular meshes and splitting each triangle into three elements. Representative meshes with similar global degrees of freedom are shown in Figure A.5. In Figure A.6, we present the convergence rates of the five stress-hybrid methods. Like the case of structured meshes, all five methods deliver optimal convergence rates on unstructured meshes, with 12β PSH-VEM followed by 9β SH-VEM delivering the lowest errors in the energy seminorm and L^2 norm of hydrostatic stress.

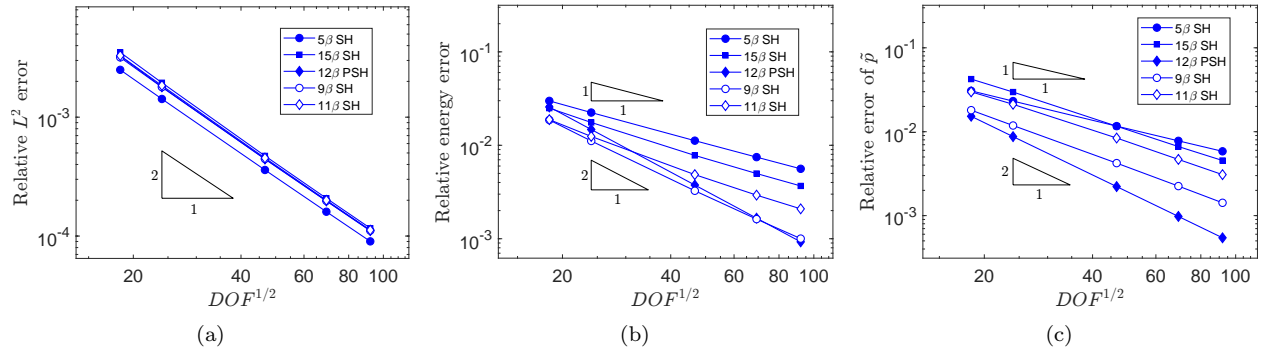


Figure A.4: Comparison of 5β SH-VEM, 15β SH-VEM, 12β PSH-VEM, 9β SH-VEM, and 11β SH-VEM for the plate with a hole problem on structured meshes. (a) L^2 error of displacement, (b) energy error, and (c) L^2 error of hydrostatic stress.

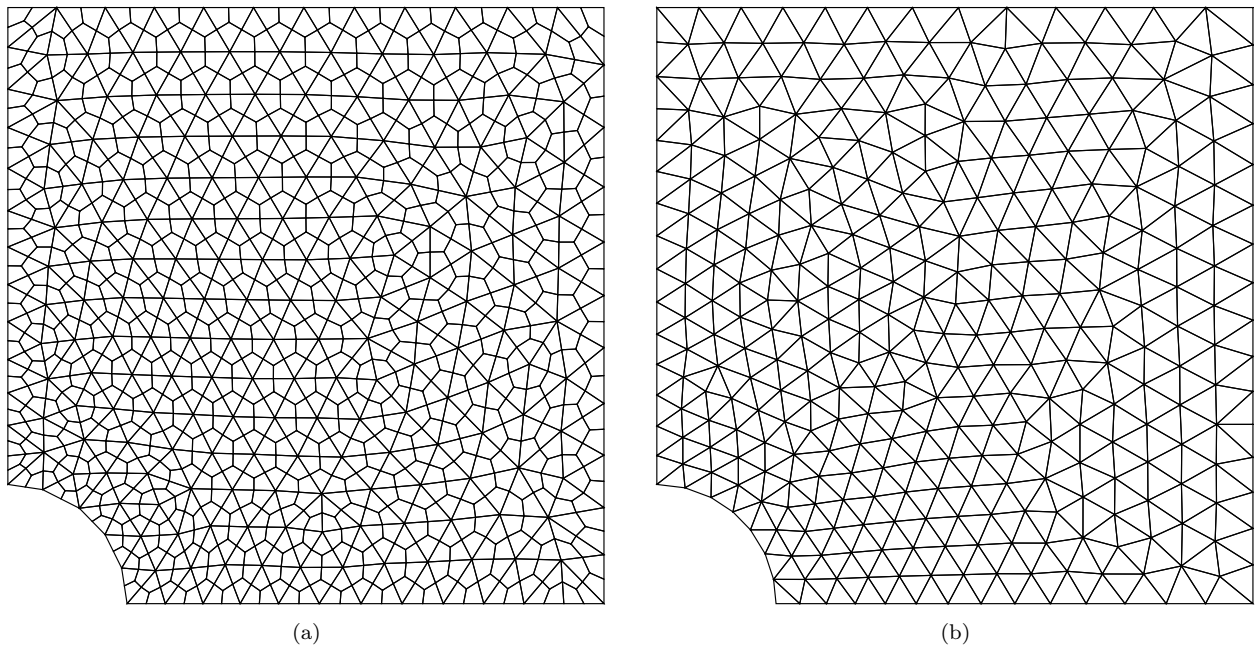


Figure A.5: (a) An unstructured quadrilateral mesh and (b) an unstructured triangular mesh with a similar number of degrees of freedom for the plate with a hole problem.

References

- [1] M. Ainsworth and C. Parker. Unlocking the secrets of locking: Finite element analysis in planar linear elasticity. *Comput Methods Appl Mech Eng*, 395:115034, 2022.
- [2] E. Artioli, L. Beirão da Veiga, C. Lovadina, and E. Sacco. Arbitrary order 2d virtual elements for polygonal meshes: part I, elastic problem. *Comput Mech*, 60(3):355–377, 2017.
- [3] E. Artioli, S. de Miranda, C. Lovadina, and L. Patruno. A family of virtual element methods for plane elasticity problems based on the Hellinger–Reissner principle. *Comput Methods Appl Mech Eng*, 340:978–999, 2018.

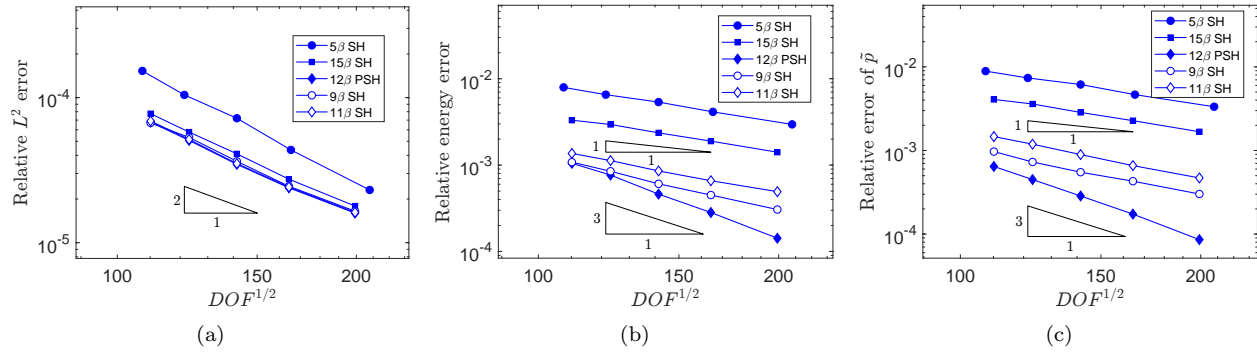


Figure A.6: Comparison of 5β SH-VEM, 15β SH-VEM, 12β PSH-VEM, 9β SH-VEM, and 11β SH-VEM for the plate with a hole problem on unstructured meshes. (a) L^2 error of displacement, (b) energy error, and (c) L^2 error of hydrostatic stress.

- [4] E. Artioli, S. de Miranda, C. Lovadina, and L. Patruno. An equilibrium-based stress recovery procedure for the VEM. *Int J Numer Methods Eng*, 117(8):885–900, 2019.
- [5] E. Artioli, S. de Miranda, C. Lovadina, and L. Patruno. A dual hybrid virtual element method for plane elasticity problems. *ESAIM: M2AN*, 54(5):1725–1750, 2020.
- [6] L. Beirão da Veiga, F. Brezzi, A. Cangiani, G. Manzini, L. D. Marini, and A. Russo. Basic principles of virtual element methods. *Math Models Methods Appl Sci*, 23:119–214, 2013.
- [7] L. Beirão da Veiga, F. Brezzi, and D. Marini. Virtual elements for linear elasticity problems. *SIAM J Numer Anal*, 51(2):794–812, 2013.
- [8] L. Beirão da Veiga, F. Brezzi, L. D. Marini, and A. Russo. The hitchhiker’s guide to the virtual element method. *Math Models Methods Appl Sci*, 24(8):1541–1573, 2014.
- [9] T. Belytschko and W. E. Bachrach. Efficient implementation of quadrilaterals with high coarse-mesh accuracy. *Comput Methods Appl Mech Eng*, 54(3):279–301, 1986.
- [10] T. Belytschko and L. Bindeman. Assumed strain stabilization of the 4-node quadrilateral with 1-point quadrature for nonlinear problems. *Comput Methods Appl Mech Eng*, 88(3):311–340, 1991.
- [11] S. Berrone, A. Borio, and F. Marcon. Lowest order stabilization free virtual element method for the 2d Poisson equation. arXiv preprint: 2103.16896, 2023.
- [12] T. Blacker and T. Belytschko. Superconvergent patch recovery with equilibrium and conjoint interpolant enhancements. *Int J Numer Methods Eng*, 37(3):517–536, 1994.
- [13] E. F. I. Boerner and P. Wriggers. A macro-element for incompressible finite deformations based on a volume averaged deformation gradient. *Comput Mech*, 42(3):407–416, 2008.
- [14] G. Camacho and M. Ortiz. Computational modelling of impact damage in brittle materials. *Int J Solids Struct*, 33(20):2899–2938, 1996.

- [15] Y. P. Cao, N. Hu, J. Lu, H. Fukunaga, and Z. H. Yao. A 3d brick element based on hu-washizu variational principle for mesh distortion. *Int J Numer Methods Eng*, 53(11): 2529–2548, 2002.
- [16] Y. P. Cao, N. Hu, H. Fukunaga, J. Lu, and Z. H. Yao. A highly accurate brick element based on a three-field variational principle for elasto-plastic analysis. *Finite Elem Anal Des*, 39(12):1155–1171, 2003.
- [17] S. Cen, X.-R. Fu, and M.-J. Zhou. 8- and 12-node plane hybrid stress-function elements immune to severely distorted mesh containing elements with concave shapes. *Comput Methods Appl Mech Eng*, 200(29):2321–2336, 2011.
- [18] A. Chen and N. Sukumar. Stabilization-free serendipity virtual element method for plane elasticity. *Comput Methods Appl Mech Eng*, 404:115784, 2023.
- [19] A. Chen and N. Sukumar. Stabilization-free virtual element method for plane elasticity. *Comput Math Applications*, 138:88–105, 2023.
- [20] A. Chen and N. Sukumar. Stress-hybrid virtual element method on quadrilateral meshes for compressible and nearly-incompressible linear elasticity. *Int J Numer Methods Eng*, 2023. DOI: <https://doi.org/10.1002/nme.7384>.
- [21] E. B. Chin and N. Sukumar. Scaled boundary cubature scheme for numerical integration over planar regions with affine and curved boundaries. *Comput Methods Appl Mech Eng*, 380:113796, 2021.
- [22] R. D. Cook. Improved two-dimensional finite element. *J Struct Div-ASCE*, 100(9): 1851–1863, 1974.
- [23] R. D. Cook. Avoidance of parasitic shear in plane element. *J Struct Div-ASCE*, 101(6): 1239–1253, 1975.
- [24] R. D. Cook. A plane hybrid element with rotational d.o.f. and adjustable stiffness. *Int J Numer Methods Eng*, 24(8):1499–1508, 1987.
- [25] R. D. Cook. Some options for plane triangular elements with rotational degrees of freedom. *Finite Elem Anal Des*, 6(3):245–249, 1990.
- [26] E. Cáceres, G. N. Gatica, and F. A. Sequeira. A mixed virtual element method for a pseudostress-based formulation of linear elasticity. *Appl Numer Math*, 135:423–442, 2019.
- [27] K. T. Danielson. Fifteen node tetrahedral elements for explicit methods in nonlinear solid dynamics. *Comput Methods Appl Mech Eng*, 272:160–180, 2014.
- [28] F. Dassi, C. Lovadina, and M. Visinoni. Hybridization of the virtual element method for linear elasticity problems. *Math Models Methods Appl Sci*, 31(14):2979–3008, 2021.
- [29] A. M. D’Altri, S. de Miranda, L. Patruno, and E. Sacco. An enhanced VEM formulation for plane elasticity. *Comput Methods Appl Mech Eng*, 376:113663, 2021.

- [30] J. Eom, J. Ko, and B. Chai Lee. A macro plane triangle element from the individual element test. *Finite Elem Anal Des*, 45(6):422–430, 2009.
- [31] C. A. Felippa. A study of optimal membrane triangles with drilling freedoms. *Comput Methods Appl Mech Eng*, 192(16):2125–2168, 2003.
- [32] J. W. Foulk III, J. T. Ostien, B. Talamini, M. R. Tupek, N. K. Crane, A. Mota, and M. G. Veilleux. Extending a 10-node composite tetrahedral finite element for solid mechanics. *Int J Numer Methods Eng*, 122(15):3845–3875, 2021.
- [33] S. Ghosh and R. Mallett. Voronoi cell finite elements. *Comput Struct*, 50(1):33–46, 1994.
- [34] Y. Guo, M. Ortiz, T. Belytschko, and E. A. Repetto. Triangular composite finite elements. *Int J Numer Methods Eng*, 47(1-3):287–316, 2000.
- [35] J. Jirousek and A. Venkatesh. Generation of optimal assumed stress expansions for hybrid-stress elements. *Comput Struct*, 32(6):1413–1417, 1989.
- [36] C. S. Jog. A 27-node hybrid brick and a 21-node hybrid wedge element for structural analysis. *Finite Elem Anal Des*, 41(11):1209–1232, 2005.
- [37] C. S. Jog. Improved hybrid elements for structural analysis. *Mech Mater*, 5:507–528, 10 2010.
- [38] C. S. Jog and P. P. Kelkar. Non-linear analysis of structures using high performance hybrid elements. *Int J Numer Methods Eng*, 68(4):473–501, 2006.
- [39] C. Kadapa. Novel quadratic Bézier triangular and tetrahedral elements using existing mesh generators: Applications to linear nearly incompressible elastostatics and implicit and explicit elastodynamics. *Int J Numer Methods Eng*, 117(5):543–573, 2019.
- [40] A. Karimipour and E. Noroozinejad Farsangi. Airy stress function for proposed thermoelastic triangular elements. *J Eng Math*, 138(1):11, 2023.
- [41] A. Lamperti, M. Cremonesi, U. Perego, A. Russo, and C. Lovadina. A Hu–Washizu variational approach to self-stabilized virtual elements: 2d linear elastostatics. *Comput Mech*, 2023.
- [42] L. Leonetti and M. Aristodemo. A composite mixed finite element model for plane structural problems. *Finite Elem Anal Des*, 94:33–46, 2015.
- [43] T. Li, X. Ma, J. Xili, and W. Chen. Higher-order hybrid stress triangular Mindlin plate element. *Comput Mech*, 58(6):911–928, 2016.
- [44] C. S. Long, S. Geyer, and A. A. Groenwold. A numerical study of the effect of penalty parameters for membrane elements with independent rotation fields and penalized equilibrium. *Finite Elem Anal Des*, 42(8):757–765, 2006.

- [45] X. Ma and W. Chen. Refined 18-dof triangular hybrid stress element for couple stress theory. *Finite Elem Anal Des*, 75:8–18, 2013.
- [46] D. S. Malkus and T. J. Hughes. Mixed finite element methods — reduced and selective integration techniques: A unification of concepts. *Comput Methods Appl Mech Eng*, 15(1):63–81, 1978.
- [47] E. A. S. Neto, F. M. A. Pires, and D. R. J. Owen. F-bar-based linear triangles and tetrahedra for finite strain analysis of nearly incompressible solids. part i: formulation and benchmarking. *Int J Numer Methods Eng*, 62(3):353–383, 2005.
- [48] H. Nguyen-Xuan, K. N. Chau, and K. N. Chau. Polytopal composite finite elements. *Comput Methods Appl Mech Eng*, 355:405–437, 2019.
- [49] K. Park, H. Chi, and G. Paulino. B-bar virtual element method for nearly incompressible and compressible materials. *Meccanica*, 56:1423–1439, 2020.
- [50] P.-O. Persson and G. Strang. A simple mesh generator in MATLAB. *SIAM Rev*, 46(2):329–345, 2004.
- [51] T. H. H. Pian. Derivation of element stiffness matrices by assumed stress distributions. *AIAA Journal*, 2(7):1333–1336, 1964.
- [52] T. H. H. Pian and K. Sumihara. Rational approach for assumed stress finite elements. *Int J Numer Methods Eng*, 20(9):1685–1695, 1984.
- [53] T. H. H. Pian and P. Tong. Relations between incompatible displacement model and hybrid stress model. *Int J Numer Methods Eng*, 22(1):173–181, 1986.
- [54] T. H. H. Pian and C.-C. Wu. A rational approach for choosing stress terms for hybrid finite element formulations. *Int J Numer Methods Eng*, 26(10):2331–2343, 1988.
- [55] R. Piltner and R. L. Taylor. A systematic construction of b-bar functions for linear and non-linear mixed-enhanced finite elements for plane elasticity problems. *Int J Numer Methods Eng*, 44(5):615–639, 1999.
- [56] B. D. Reddy and D. van Huyssteen. A virtual element method for transversely isotropic elasticity. *Comput Mech*, 64(4):971–988, 2019.
- [57] M. Rezaiee-Pajand and A. Karimipour. Three stress-based triangular elements. *Eng Comput*, 36(4):1325–1345, 2020.
- [58] G. Scovazzi, B. Carnes, X. Zeng, and S. Rossi. A simple, stable, and accurate linear tetrahedral finite element for transient, nearly, and fully incompressible solid dynamics: a dynamic variational multiscale approach. *Int J Numer Methods Eng*, 106(10):799–839, 2016.
- [59] T. Shilt, P. J. O’Hara, R. Deshmukh, and J. J. McNamara. Solution of nearly incompressible field problems using a generalized finite element approach. *Comput Methods Appl Mech Eng*, 368:113165, 2020.

- [60] J. Simo, F. Armero, and R. Taylor. Improved versions of assumed enhanced strain trilinear elements for 3d finite deformation problems. *Comput Methods Appl Mech Eng*, 110(3):359–386, 1993.
- [61] J. C. Simo and T. J. R. Hughes. On the variational foundations of assumed strain methods. *J Appl Mech*, 53(1):51–54, 1986.
- [62] J. C. Simo and M. S. Rifai. A class of mixed assumed strain methods and the method of incompatible modes. *Int J Numer Methods Eng*, 29(8):1595–1638, 1990.
- [63] R. L. Spilker. Improved hybrid-stress axisymmetric elements including behaviour for nearly incompressible materials. *Int J Numer Methods Eng*, 17(4):483–501, 1981.
- [64] R. L. Spilker, S. M. Maskeri, and E. Kania. Plane isoparametric hybrid-stress elements: Invariance and optimal sampling. *Int J Numer Methods Eng*, 17(10):1469–1496, 1981.
- [65] K. Y. Sze. On immunizing five-beta hybrid-stress element models from ‘trapezoidal locking’ in practical analyses. *Int J Numer Methods Eng*, 47(4):907–920, 2000.
- [66] P. Thoutireddy, J. F. Molinari, E. A. Repetto, and M. Ortiz. Tetrahedral composite finite elements. *Int J Numer Methods Eng*, 53(6):1337–1351, 2002.
- [67] S. P. Timoshenko and J. N. Goodier. *Theory of Elasticity*. McGraw-Hill, New York, third edition, 1970.
- [68] C. Wang, X. Zhang, and P. Hu. Assumed stress quasi-conforming triangular element for couple stress theory. *Acta Mech Solida Sin*, 30(4):335–344, 2017.
- [69] N.-E. Wiberg and F. Abdulwahab. Patch recovery based on superconvergent derivatives and equilibrium. *Int J Numer Methods Eng*, 36(16):2703–2724, 1993.
- [70] E. L. Wilson, R. L. Taylor, W. P. Doherty, and J. Ghaboussi. Incompatible displacement models. In S. J. Fenves, N. Perrone, A. R. Robinson, and W. C. Schnobrich, editors, *Numerical and Computer Methods in Structural Mechanics*, pages 43–57. Elsevier, 1973.
- [71] P. Wriggers, B. D. Reddy, W. Rust, and B. Hudobivnik. Efficient virtual element formulations for compressible and incompressible finite deformations. *Comput Mech*, 60(2):253–268, 2017.
- [72] C.-C. Wu and Y. Cheung. On optimization approaches of hybrid stress elements. *Finite Elem Anal Des*, 21(1):111–128, 1995.
- [73] C.-C. Wu and Y. K. Cheung. Penalty-equilibrating approach and an innovative formulation of 4-noded hybrid stress elements. *Commun Numer Meth En*, 12(11):707–717, 1996.
- [74] Q. Xiao, B. Karihaloo, and F. Williams. Application of penalty-equilibrium hybrid stress element method to crack problems. *Eng Fract Mech*, 63(1):1–22, 1999.

- [75] O. C. Zienkiewicz. Displacement and equilibrium models in the finite element method by B. Fraeijs de Veubeke, chapter 9, pages 145–197 of *Stress Analysis*, edited by O. C. Zienkiewicz and G. S. Holister, published by John Wiley & Sons, 1965. *Int J Numer Methods Eng*, 52(3):287–342, 2001.